Computational Mechanics manuscript No.
(will be inserted by the editor)

A smoothed finite element approach for computational fluid dynamics: Applications to incompressible flows and fluid–structure interaction

Tao He · Hexin Zhang · Kai Zhang

Received: date / Accepted: date

Abstract In this paper the cell-based smoothed finite element method (CS-FEM) is introduced into two mainstream aspects of computational fluid dynamics: incompressible flows and fluid–structure interaction (FSI). The emphasis is placed on the fluid gradient smoothing which simply requires equal numbers of Gaussian points and smoothing cells in each four-node quadrilateral element. The second-order, smoothed characteristic-based split scheme in conjunction with a pressure stabilization is then presented to settle the incompressible Navier–Stoke equations. As for FSI, CS-FEM is applied to the geometrically nonlinear solid as usual. Following an efficient mesh deformation strategy, block-Gauss–Seidel procedure is adopted to couple all individual fields under the arbitrary Lagriangian–Eulerian description. The proposed solvers are carefully validated against the previously published data for several benchmarks, revealing visible improvements in computed results.

Keywords Smoothed finite element method · CFD · Incompressible flows · Fluid-structure interaction · Characteristic-based split · ALE

1 Introduction

Computational fluid dynamics (CFD) is a modern discipline concerned with mathematical modeling, numerical methods and software tools of fluid dynamics. The

T. He
Department of Civil Engineering, Shanghai Normal University, Shanghai 201418, China
School of Engineering, University of Birmingham, Birmingham B15 2TT, UK E-mail: taohe@shnu.edu.cn

H.-X. Zhang
School of Engineering and the Built Environment, Edinburgh Napier University, Edinburgh EH10 5DT, UK
E-mail: j.zhang@napier.ac.uk

K. Zhang
Department of Civil Engineering, Graduate School of Urban Innovation, Yokohama National University, Yokohama 2408501, Japan
E-mail: kai-zhang-kf@ynu.jp

principle of the majority of CFD problems relies on the Navier–Stokes (NS) equations which describe how different variants (e.g. the velocity, pressure, temperature and density) of a moving fluid are related and predict what is the flow state physically. As a matter of fact, the numerical resolution of these balance equations (with moving and deformable boundaries) has drawn a substantial amount of endeavors from both scientific and engineering communities. Under the umbrella of this major branch, finite element method (FEM) is widely utilized for analysis and design of a variety of specializations like incompressible flows past bluff/streamlined bodies [63,78] and fluid–structure interaction (FSI) [58,4]. Normally, the standard Galerkin finite element procedure for incompressible flows is confronted with two sources of numerical instabilities [63]. One source is due to the presence of the convective acceleration in the NS equations, mainly causing spurious oscillations in the velocity field. The other source rests with the inappropriate usage of a pair of interpolation functions for velocity and pressure fields, which primarily poses the pressure oscillations. In the past decades, a number of stabilized FEMs have been successfully devised to prevent these potential instabilities. Popular approaches contain streamline upwind/Petrov–Galerkin (SUPG) formulation [8], Taylor–Galerkin method [18], Galerkin/least-squares (GLS) technique [35], pressure-stabilized Petrov–Galerkin (PSPG) formulation [66], space–time FEM [64,65,59,60,57], characteristic-based split (CBS) scheme [77,53], etc. Nowadays FEM has become one of stable and robust numerical methodologies for solving CFD related problems and delivering deep insights into fluid physics. For example, the complex three-dimensional turbocharger flow is handled by the space-time variational multiscale FEM incorporating isogeometric analysis [60].

Typical finite element solution results in a system of algebraic equations, which approximates the original partial differential equations (PDEs) based upon a finite element discretization. During the process, we probably observe the *overly-stiff* phenomenon owing to the fully compatible strain field [49]. In examining meshless and finite element methods, Liu and his colleagues [48] found *gradient smoothing* [9,71] an elegant remedy to the afore-mentioned overly-stiff issue, as well as a valuable alliance of these two methods. In the seminal publication [48], the smoothed finite element method (SFEM) is proposed by incorporating gradient smoothing operation with the traditional FEM. The essential idea behind SFEM lies in modification of the compatible strain field whereby a Galerkin model may deliver some superior properties. This method is saliently featured with the *softened* stiffness matrix that yields more accurate solution to discrete PDEs than the standard FEM. After a decade of development, a group of SFEM models has been fostered with versatile applications in solid mechanics, heat transfer and acoustics whose governing equations perfectly suit the technique after introducing divergence theorem. The reader is referred to the monograph [49] and the review article [72] for the state of the art of SFEM.

In recent years, SFEM has seemingly been applied into a range of FSI problems as follows. The immersed SFEM is developed in [75,73,70,74] where SFEM is responsible for nonlinear solids. Wang *et al.* [68] integrated SFEM in solid mechanics with a strong-form fluid solver under the arbitrary Lagrangian–Eulerian (ALE) description [34]. Similarly, the authors adopted SFEM to quantify the structural finite deformation triggered by fluidic excitation in a partitioned manner [24,27, 28,30]. However, these scenarios do not provide any settlements tailored for the NS equations, but rather replicate SFEM's early success in solid mechanics.

The major dilemma that SFEM faces in CFD stems from interpolating the mixed product of a quantity and its gradient in the NS equations, such as the convective acceleration. For this reason, the underlying investments may be discouraged from CFD. Most recently, we have witnessed a joyful breakthrough that makes the cell-based smoothed FEM (CS-FEM) accessible to incompressible NS equations in terms of three schemes to interpolate nodal quantities involving the mixed product [38].

This work is motivated by the need for a broadening utilization of SFEM for CFD. A natural preference is given to the simplest CS-FEM that is initiated on the basis of bilinear four-node quadrilateral (Q4) element. The easy smoothing treatment is proposed for the fluid equations to bypass the strenuous operations. For this purpose, we set up the equal amounts of Gaussian points (GPs) and smoothing cells (SCs) in each element to compute fluid fluxes. That is to say, the contribution from all SCs is accumulated in the loop circulating the Gaussian integration. As a result of this collective effort, a second-order smoothed CBS (S-CBS) scheme with the stabilized pressure gradient projection (SPGP) technique [12,54, 1,6] is utilized to decouple the fluid velocity and pressure. As to FSI, the nonlinear block-Gauss–Seidel procedure [26,25] is preferred to interconnect individual fields owing to its attractive simplicity with good convergence. In short, the marriage of SFEM and fractional-step method may soothe the pressure fluctuation on (dynamic) boundaries. This is potentially important to both incompressible flows and FSI simulations.

The remainder of this paper is organized as follows. The theory of CS-FEM is briefly recalled in Section 2. The ALE form of fluid governing equations is given in Section 3 while the structural dynamics is depicted in Section 4. The mesh updating method is described in Section 5. Subsequently, Section 6 explains the partitioned coupling algorithm in detail. Several benchmark examples are investigated in Section 7. Concluding remarks are drawn in the final section.

2 Fundamental basis of CS-FEM

We discretize a two-dimensional computational domain Ω into n_{e} Q4 elements such that $\Omega = \Omega_1 \cup \Omega_2 \cup \cdots \cup \Omega_{n_{\mathrm{e}}}$ and $\Omega_i \cap \Omega_j = \varnothing$ $(i \neq j)$. A Q4 element is subdivided into a set of complementary SCs, i.e. $\Omega_i = \widetilde{\Omega}_i^1 \cup \widetilde{\Omega}_i^2 \cup \cdots \cup \widetilde{\Omega}_i^{n_{\mathrm{c}}}$ where n_{c} is the number of SCs in the i-th element. As illustrated in Fig. 1, the smoothed gradient of a field variable b at a point $\mathbf{x}_{\mathrm{c}}$ in an SC is approximated by

$$\widetilde{\nabla} b(\mathbf{x}_{\mathrm{c}}) = \int_{\widetilde{\Omega}} \nabla b(\mathbf{x}) W(\mathbf{x} - \mathbf{x}_{\mathrm{c}}) \mathrm{d}\Omega, \tag{1}$$

where ∇ means the gradient operator and $\widetilde{\nabla}$ is its smoothed counterpart, $\widetilde{\Omega}$ designates the SC and W is the Heaviside-type kernel that possesses the following properties [71]

$$W(\mathbf{x} - \mathbf{x}_{\mathrm{c}}) \geqslant 0 \quad \text{and} \quad \int_{\widetilde{\Omega}} W(\mathbf{x} - \mathbf{x}_{\mathrm{c}}) \mathrm{d}\Omega = 1. \tag{2}$$

Applying Gauss theorem into the right-hand side of Eq. (1) yields

$$\widetilde{\nabla} b(\mathbf{x}_{\mathrm{c}}) = \int_{\widetilde{\Gamma}} b(\mathbf{x}) \mathbf{n}(\mathbf{x}) W(\mathbf{x} - \mathbf{x}_{\mathrm{c}}) \mathrm{d}\Gamma - \int_{\widetilde{\Omega}} b(\mathbf{x}) \nabla W(\mathbf{x} - \mathbf{x}_{\mathrm{c}}) \mathrm{d}\Omega, \tag{3}$$

where $\widetilde{\Gamma}$ is the boundary of $\widetilde{\Omega}$ and $\mathbf{n}$ is the unit outward normal of $\widetilde{\Gamma}$. A piecewise constant kernel W is now formulated in form of

$$W(\mathbf{x}-\mathbf{x}_{\mathrm{c}})=\begin{cases}\dfrac{1}{A_{\mathrm{c}}} & \mathbf{x}\in\widetilde{\Omega},\\ 0 & \mathbf{x}\notin\widetilde{\Omega},\end{cases} \tag{4}$$

where $A_{\mathrm{c}}=\int_{\widetilde{\Omega}}\mathrm{d}\Omega$ is the area of the SC. Substituting Eq. (4) into Eq. (3), we have

$$\widetilde{\nabla}b(\mathbf{x}_{\mathrm{c}})=\int_{\widetilde{\Gamma}}b(\mathbf{x})\mathbf{n}(\mathbf{x})W(\mathbf{x}-\mathbf{x}_{\mathrm{c}})\mathrm{d}\Gamma=\frac{1}{A_{\mathrm{c}}}\int_{\widetilde{\Gamma}}b(\mathbf{x})\mathbf{n}(\mathbf{x})\mathrm{d}\Gamma, \tag{5}$$

where the gradient of a constant vanishes automatically.

The Galerkin procedure leads to the following approximation of b

$$b=N_I\bar{b}_I, \tag{6}$$

where N_I is the shape function at node I, the bar indicates a nodal quantity and Einstein summation convention is applied. With the aid of Eq. (6), Eq. (5) is rewritten as

$$\widetilde{\nabla}b(\mathbf{x}_{\mathrm{c}})=\left(\widetilde{\nabla}N_I(\mathbf{x}_{\mathrm{c}})\right)\bar{b}_I=\left(\frac{1}{A_{\mathrm{c}}}\int_{\widetilde{\Gamma}}N_I(\mathbf{x})\mathbf{n}(\mathbf{x})\mathrm{d}\Gamma\right)\bar{b}_I. \tag{7}$$

Since one-point Gaussian quadrature is sufficiently accurate for two-node line integral, the item enclosed within external brackets on the right-hand side of Eq. (7) can be transformed to its algebraic form

$$\widetilde{\nabla}N_I(\mathbf{x}_{\mathrm{c}})=\frac{1}{A_{\mathrm{c}}}\sum_{i=1}^{4}N_I(\mathbf{x}_i^{\mathrm{gp}})\mathbf{n}(\mathbf{x}_i^{\mathrm{gp}})l_i, \tag{8}$$

where 4 indicates the number of segments per quadrilateral SC, $\mathbf{x}_i^{\mathrm{gp}}$ is the GP on the i-th segment $\widetilde{\Gamma}_i$ and l_i is the length of $\widetilde{\Gamma}_i$.

By now, no coordinate transformation is involved in the gradient smoothing process such that a heavily distorted mesh is possibly accommodated [48]. Furthermore, the imported smoothing concept may pass on to wet boundaries the improved traction or pressure. The construction of shape functions for CS-FEM is shown in Fig. 2. A Q4 element is partitioned into four quadrilateral SCs in consideration of the stability condition [48]. Of total nine nodes, extra five nodes are generated to compute the smoothed shape functions by simply averaging those values at four corners [48, 14].

3 Incompressible fluid flow

3.1 Governing equations

Without loss of generality, the NS equations governing an isothermal incompressible viscous fluid flow on a time-dependent domain $\Omega^{\mathrm{f}}\subset\mathbb{R}^2$ in a time interval $(0,\ T)$ are written in their ALE formulation of

$$\nabla\cdot\mathbf{u}=0\quad\text{on}\quad\Omega^{\mathrm{f}}\times(0,\ T), \tag{9}$$

$$\rho^{\mathrm{f}}\left(\frac{\partial \mathbf{u}}{\partial t}+\mathbf{c}\cdot\nabla\mathbf{u}-\mathbf{f}^{\mathrm{f}}\right)-\nabla\cdot\boldsymbol{\sigma}^{\mathrm{f}}=\mathbf{0}\quad\text{on}\quad\Omega^{\mathrm{f}}\times(0,\ T),\tag{10}$$

where $\mathbf{u}$ is the fluid velocity, ρ^{f} is the fluid density, $\mathbf{c}=\mathbf{u}-\mathbf{w}$ is the convective velocity, $\mathbf{w}$ is the mesh velocity, $\mathbf{f}^{\mathrm{f}}$ is the fluid body force and $\boldsymbol{\sigma}^{\mathrm{f}}$ is the fluid stress tensor. For the Eulerian flows, we have $\mathbf{w}=\mathbf{0}$ such that $\mathbf{c}$ degenerates into $\mathbf{u}$.

The constitutive equation for Newtonian fluid reads as

$$\boldsymbol{\sigma}^{\mathrm{f}}=-p\mathbf{I}+2\mu\boldsymbol{\epsilon}\quad\text{and}\quad\boldsymbol{\epsilon}=\frac{1}{2}\left(\nabla\mathbf{u}+(\nabla\mathbf{u})^{\mathrm{T}}\right)\quad\text{on}\quad\Omega^{\mathrm{f}}\times(0,\ T),\tag{11}$$

where p is the pressure, $\mathbf{I}$ denotes the identity tensor, μ is the dynamic viscosity, $\boldsymbol{\epsilon}$ indicates the rate-of-strain tensor and superscript T means transpose.

It is assumed that proper boundary conditions (abbreviated to BCs) are imposed at different segments of the domain boundary Γ^{f} below

$$\mathbf{u}=\mathbf{g}^{\mathrm{f}}\quad\text{on}\quad\Gamma^{\mathrm{f}}_{\mathrm{d}},\quad\boldsymbol{\sigma}^{\mathrm{f}}\cdot\mathbf{n}^{\mathrm{f}}=\mathbf{h}^{\mathrm{f}}\quad\text{on}\quad\Gamma^{\mathrm{f}}_{\mathrm{n}},\tag{12}$$

where $\Gamma^{\mathrm{f}}_{\mathrm{d}}$ and $\Gamma^{\mathrm{f}}_{\mathrm{n}}$ designate the Dirichlet and Neumann sub-boundaries, respectively, and $\mathbf{n}^{\mathrm{f}}$ is the unit outward normal of $\Gamma^{\mathrm{f}}_{\mathrm{n}}$. The fluid problem is initiated by prescribing initial conditions as follows

$$\mathbf{u}(\mathbf{x},\ t=0)=\mathbf{u}^{0},\quad p(\mathbf{x},\ t=0)=p^{0}\quad\text{on}\quad\Omega^{\mathrm{f}}_{0},\tag{13}$$

where $\mathbf{x}$ and t, of course, represent the spatial and temporal coordinates, respectively. The coupling conditions on fluid–structure interface Σ will be presented in a separate subsection.

In view of the characteristic length L and the free-stream velocity U, we define the dimensionless scales

$$\hat{\mathbf{x}}=\frac{\mathbf{x}}{L},\ \hat{t}=\frac{tU}{L},\ \hat{\mathbf{u}}=\frac{\mathbf{u}}{U},\ \hat{\mathbf{c}}=\frac{\mathbf{c}}{U},\ \hat{p}=\frac{p}{\rho^{\mathrm{f}}U^{2}},\ \hat{\mathbf{f}}^{\mathrm{f}}=\frac{\mathbf{f}^{\mathrm{f}}L}{U^{2}}$$

to develop the dimensionless ALE–NS equations

$$\nabla\cdot\mathbf{u}=0,\tag{14}$$

$$\frac{\partial \mathbf{u}}{\partial t}+\mathbf{c}\cdot\nabla\mathbf{u}-\nabla\cdot\boldsymbol{\sigma}^{\mathrm{f}}-\mathbf{f}^{\mathrm{f}}=\mathbf{0},\tag{15}$$

along with the constitutive relation

$$\boldsymbol{\sigma}^{\mathrm{f}}=-p\mathbf{I}+\frac{1}{Re}\left(\nabla\mathbf{u}+(\nabla\mathbf{u})^{\mathrm{T}}\right),\tag{16}$$

where $Re=\rho^{\mathrm{f}}UL/\mu$ is the Reynolds number and all hats are dropped. The nondimensionalized BCs and initial conditions share the same form as Eqs. (12) and (13).

3.2 Solution procedure

The CBS scheme [77, 53] combines the characteristic Galerkin method [50] with the fractional-step method [10, 62]. The former process suppresses spurious oscillations via higher-order time stepping in the convection-dominated flows whereas the latter procedure stabilizes the pressure field. The second-order pressure splitting error can be guaranteed by inclusion of the pressure gradient, but the increased accuracy inevitably imperils the stabilizing properties of the original first-order scheme [12, 54]. In what follows, the additional SPGP stabilization [12] is introduced to overcome this penalty.

An auxiliary equation in regard to the variable $\mathbf{q}$

$$\mathbf{q} - \nabla p = \mathbf{0}, \tag{17}$$

is defined, whereby the continuity equation (14) is modified as

$$\nabla \cdot \mathbf{u} + \phi \nabla \cdot \mathbf{q} - \phi \nabla^2 p = 0, \tag{18}$$

with ϕ denoting the stabilization parameter. We will numerically discuss ϕ later as it is yet unclear how to exactly determine the parameter in theory [12].

The temporal discrete version of Eqs. (18), (15) and (17) may be written as

$$\nabla \cdot \mathbf{u}^{n+1} + \phi \nabla \cdot \mathbf{q}^n - \phi \nabla^2 p^{n+1} = 0, \tag{19}$$

$$\frac{\mathbf{u}^{n+1} - \mathbf{u}^n}{\Delta t} = -\mathbf{c}^n \cdot \nabla \mathbf{u}^n - \nabla p^{n+1} + \nabla p^n - \nabla p^n + \frac{1}{Re} \nabla^2 \mathbf{u}^n + (\mathbf{f}^{\mathrm{f}})^n, \tag{20}$$

$$\mathbf{q}^{n+1} - \nabla p^{n+1} = \mathbf{0}, \tag{21}$$

where superscript n denotes the n-th time slice and $\Delta t = t^{n+1} - t^n$ is the time step. The auxiliary variable $\mathbf{q}$ is explicitly treated in Eq. (19) while the pressue of Eq. (20) is temporally discretized in the semi-implicit manner.

Following the CBS procedure, Eq. (20) admits the decomposition below

$$\frac{\mathbf{u}^* - \mathbf{u}^n}{\Delta t} = -\mathbf{c}^n \cdot \nabla \mathbf{u}^n - \nabla p^n + \frac{1}{Re} \nabla^2 \mathbf{u}^n + \frac{\Delta t}{2} \mathbf{c}^n \cdot \nabla (\mathbf{c}^n \cdot \nabla \mathbf{u}^n + \nabla p^n), \tag{22}$$

$$\frac{\mathbf{u}^{n+1} - \mathbf{u}^*}{\Delta t} = -\nabla (p^{n+1} - p^n) + \frac{\Delta t}{2} \mathbf{c}^n \cdot \nabla^2 (p^{n+1} - p^n), \tag{23}$$

where $\mathbf{u}^*$ signifies the intermediate velocity, and the body force and the third-order terms are neglected.

Taking the divergence of Eq. (23) and expanding the semi-discrete form of Eq. (19) at the next time level yield

$$(\Delta t + \phi) \nabla^2 p^{n+1} = \nabla \cdot \mathbf{u}^* + \Delta t \nabla^2 p^n + \phi \nabla \cdot \mathbf{q}^n, \tag{24}$$

where the third-order terms are discarded as well.

With introduction of the gradient smoothing, the main steps of the stabilized second-order S-CBS scheme are arranged below

Step 1: Predict the velocity field

$$\mathbf{u}^* - \mathbf{u}^n = \Delta t \left(-\mathbf{c}^n \cdot \widetilde{\nabla} \mathbf{u}^n - \widetilde{\nabla} p^n + \frac{1}{Re} \widetilde{\nabla}^2 \mathbf{u}^n + \frac{\Delta t}{2} \mathbf{c}^n \cdot \widetilde{\nabla} (\mathbf{c}^n \cdot \widetilde{\nabla} \mathbf{u}^n + \widetilde{\nabla} p^n) \right), \tag{25}$$

Step 2: Update the pressure field

$$\widetilde{\nabla}^2 p^{n+1} = \frac{1}{\Delta t + \phi}\left(\widetilde{\nabla}\cdot\mathbf{u}^* + \Delta t\widetilde{\nabla}^2 p^n + \phi\widetilde{\nabla}\cdot\mathbf{q}^n\right), \tag{26}$$

Step 3: Correct the velocity field

$$\mathbf{u}^{n+1} - \mathbf{u}^* = -\Delta t\left(\widetilde{\nabla}(p^{n+1} - p^n) - \frac{\Delta t}{2}\mathbf{c}^n\cdot\widetilde{\nabla}^2(p^{n+1} - p^n)\right), \tag{27}$$

Step 4: Renew the auxiliary variable

$$\mathbf{q}^{n+1} = \widetilde{\nabla} p^{n+1}. \tag{28}$$

Imposition of BCs is straightforward: the velocity BCs are prescribed for Steps 1 and 3 on $\Gamma_{\mathrm{u}}^{\mathrm{f}}$, while the pressure BC for Step 2 on $\Gamma_{\mathrm{p}}^{\mathrm{f}}$. Besides, $\mathbf{q}_2 = \mathbf{0}$ is applied on the pressure-free outlet for Step 4.

3.3 Time-step limitations

It is of interest to remark that the semi-implicit CBS scheme is conditionally stable [78]. The general time-step limitations are recommended as [78,53]

$$\Delta t \leqslant \Delta t_{\mathrm{crit}} = \min(\Delta t_{\mathrm{conv}},\ \Delta t_{\mathrm{diff}}), \tag{29}$$

where Δt_{crit} signifies the critical time step, and Δt_{conv} and Δt_{diff} are the convection and diffusion limits, respectively. The latter two velocities are calculated from

$$\Delta t_{\mathrm{conv}} = \frac{h}{|\mathbf{u}|}, \quad \Delta t_{\mathrm{diff}} = \frac{1}{2}h^2 Re, \tag{30}$$

where h means the characteristic size of the element.

To account for the stability and convergence, Codina [12] advocated that the pressure stabilization parameter must satisfy the following relationship

$$\phi \leqslant \frac{1}{4}h^2 Re, \tag{31}$$

for viscous dominated flows on the Eulerian mesh. By inspecting Eq. (30), we may reconsider the inequality as

$$\phi \leqslant \frac{1}{2}\Delta t_{\mathrm{diff}}. \tag{32}$$

Recalling Eq. (29), the range of the stabilization parameter is suggested as

$$\phi \leqslant 0.5\Delta t_{\mathrm{crit}}, \tag{33}$$

or, it may be replaced for safety by

$$\phi \leqslant 0.5\Delta t. \tag{34}$$

3.4 Finite element discretization

The standard Galerkin spatial approximation is performed to discretize the fluid equations in space. Since the CBS scheme permits the equal-/low-order interpolation for both velocity and pressure, the two primitive variables are approximated as

$$\mathbf{u} = \mathbf{N}\bar{\mathbf{u}},\ p = \mathbf{N}\bar{\mathbf{p}}, \tag{35}$$

where $\mathbf{N}$ designates the shape function of Q4 element. Substitution of spatial approximation (35) into the semi-discrete form of Eqs. (25)–(28) entails the final matrix form

$$\mathbf{M}^{\mathrm{f}}(\bar{\mathbf{u}}^{*} - \bar{\mathbf{u}}^{n}) = -\Delta t\left(\widetilde{\mathbf{C}}_{\mathrm{u}}^{n}\bar{\mathbf{u}}^{n} + \widetilde{\mathbf{G}}\bar{\mathbf{p}}^{n} + \widetilde{\mathbf{K}}_{\tau}\bar{\mathbf{u}}^{n} + \frac{\Delta t}{2}(\widetilde{\mathbf{K}}_{\mathrm{u}}^{n}\bar{\mathbf{u}}^{n} + \widetilde{\mathbf{Q}}^{n}\bar{\mathbf{p}}^{n}) - \mathbf{f}_{\mathrm{u}}^{n}\right), \tag{36}$$

$$\widetilde{\mathbf{H}}\bar{\mathbf{p}}^{n+1} = -\frac{1}{\Delta t + \phi}\left(\widetilde{\mathbf{G}}\bar{\mathbf{u}}^{*} - \Delta t(\widetilde{\mathbf{H}}\bar{\mathbf{p}}^{n} - \mathbf{f}_{\mathrm{p}}^{n}) + \phi\widetilde{\mathbf{G}}\bar{\mathbf{q}}^{n}\right) + \mathbf{f}_{\mathrm{p}}^{n+1}, \tag{37}$$

$$\mathbf{M}^{\mathrm{f}}(\bar{\mathbf{u}}^{n+1} - \bar{\mathbf{u}}^{*}) = -\Delta t\left(\widetilde{\mathbf{G}}^{\mathrm{T}}(\bar{\mathbf{p}}^{n+1} - \bar{\mathbf{p}}^{n}) + \frac{\Delta t}{2}\widetilde{\mathbf{Q}}^{n}(\bar{\mathbf{p}}^{n+1} - \bar{\mathbf{p}}^{n}) + \check{\mathbf{f}}_{\mathrm{p}}^{n}\right), \tag{38}$$

$$\mathbf{M}^{\mathrm{f}}\bar{\mathbf{q}}^{n+1} = \widetilde{\mathbf{G}}^{\mathrm{T}}\bar{\mathbf{p}}^{n+1}, \tag{39}$$

where the assembled matrices and vectors are presented below

$$\mathbf{M}^{\mathrm{f}} = \int_{\Omega^{\mathrm{f}}}\mathbf{N}^{\mathrm{T}}\mathbf{N}\mathrm{d}\Omega,\ \widetilde{\mathbf{H}} = \int_{\Omega^{\mathrm{f}}}(\widetilde{\nabla}\mathbf{N})^{\mathrm{T}}(\widetilde{\nabla}\mathbf{N})\mathrm{d}\Omega,$$

$$\widetilde{\mathbf{C}}_{\mathrm{u}}^{n} = \int_{\Omega^{\mathrm{f}}}\mathbf{N}^{\mathrm{T}}(\widetilde{\nabla}^{\mathrm{T}}\mathbf{c}^{n}\mathbf{N})\mathrm{d}\Omega,\ \widetilde{\mathbf{G}} = \int_{\Omega^{\mathrm{f}}}(\widetilde{\nabla}\mathbf{N})^{\mathrm{T}}\mathbf{N}\mathrm{d}\Omega,\ \widetilde{\mathbf{K}}_{\tau} = \frac{1}{Re}\int_{\Omega^{\mathrm{f}}}(\widetilde{\nabla}\mathbf{N})^{\mathrm{T}}(\widetilde{\nabla}\mathbf{N})\mathrm{d}\Omega,$$

$$\widetilde{\mathbf{K}}_{\mathrm{u}}^{n} = \int_{\Omega^{\mathrm{f}}}(\widetilde{\nabla}^{\mathrm{T}}\mathbf{c}^{n}\mathbf{N})^{\mathrm{T}}(\widetilde{\nabla}^{\mathrm{T}}\mathbf{c}^{n}\mathbf{N})\mathrm{d}\Omega,\ \widetilde{\mathbf{Q}}^{n} = \int_{\Omega^{\mathrm{f}}}(\widetilde{\nabla}^{\mathrm{T}}\mathbf{c}^{n}\mathbf{N})^{\mathrm{T}}(\widetilde{\nabla}\mathbf{N})\mathrm{d}\Omega,$$

$$\mathbf{f}_{\mathrm{u}}^{n} = \frac{1}{Re}\int_{\Gamma^{\mathrm{f}}}\mathbf{N}^{\mathrm{T}}\mathbf{n}^{\mathrm{T}}(\nabla^{\mathrm{T}}\mathbf{u}^{n})\mathrm{d}\Gamma + \frac{\Delta t}{2}\int_{\Gamma^{\mathrm{f}}}\mathbf{N}^{\mathrm{T}}(\mathbf{n}^{\mathrm{T}}\mathbf{c}^{n})(\nabla^{\mathrm{T}}\mathbf{c}^{n}\mathbf{u}^{n} + \nabla p)\mathrm{d}\Gamma,$$

$$\mathbf{f}_{\mathrm{p}}^{n} = \int_{\Gamma^{\mathrm{f}}}\mathbf{N}^{\mathrm{T}}(\mathbf{n}^{\mathrm{T}}\nabla p^{n})\mathrm{d}\Gamma,\ \check{\mathbf{f}}_{\mathrm{p}}^{n} = \frac{\Delta t}{2}\int_{\Gamma^{\mathrm{f}}}\mathbf{N}^{\mathrm{T}}(\mathbf{n}^{\mathrm{T}}\mathbf{c}^{n})\nabla(p^{n+1} - p^{n})\mathrm{d}\Gamma.$$

At a closer observation of the above representation, the two smoothed element matrices being derivated from the second derivatives are directly finalized by assembly of all SCs of the element e, i.e.,

$${}^{e}\widetilde{\mathbf{H}} = \int_{\Omega_{e}^{\mathrm{f}}}(\widetilde{\nabla}\mathbf{N})^{\mathrm{T}}(\widetilde{\nabla}\mathbf{N})\mathrm{d}\Omega = \sum_{i=1}^{n_{\mathrm{c}}}(\widetilde{\nabla}\mathbf{N})_{i}^{\mathrm{T}}(\widetilde{\nabla}\mathbf{N})_{i}A_{\mathrm{c}}^{i}, \tag{40a}$$

$${}^{e}\widetilde{\mathbf{K}}_{\tau} = \frac{1}{Re}\int_{\Omega_{e}^{\mathrm{f}}}(\widetilde{\nabla}\mathbf{N})^{\mathrm{T}}(\widetilde{\nabla}\mathbf{N})\mathrm{d}\Omega = \frac{1}{Re}\sum_{i=1}^{n_{\mathrm{c}}}(\widetilde{\nabla}\mathbf{N})_{i}^{\mathrm{T}}(\widetilde{\nabla}\mathbf{N})_{i}A_{\mathrm{c}}^{i}. \tag{40b}$$

The remaining smoothed element matrices manifest themselves in the mixed product of a quantity and its first derivative, see ${}^{e}\widetilde{\mathbf{G}}$ for example. To handle those items, we simply dictate that the number and numbering of GPs per Q4 element

exactly equal to those of SCs. Since 2×2 GPs in Q4-FEM and $n_{\mathrm{c}} = 4$ in CS-FEM are often adopted in practice, it is straightforward to estimate ${}^{e}\widetilde{\mathbf{G}}$ below

$$ {}^{e}\widetilde{\mathbf{G}} = \int_{\Omega^{\mathrm{f}}} (\widetilde{\nabla}\mathbf{N})^{\mathrm{T}} \mathbf{N} \mathrm{d}\Omega = \sum_{i=1}^{2} \sum_{j=1}^{2} (\widetilde{\nabla}\mathbf{N})_{ij}^{\mathrm{T}} \mathbf{N}(\mathbf{x}_{ij}^{\mathrm{gp}}) A_{\mathrm{c}}^{ij}. \tag{41} $$

As can be seen from Fig. 3, the contribution of four SCs and GPs per Q4 element successfully circulates within one recurrence. Compared to [38], we organize the smoothed element integral into a more comprehensible pattern.

4 Structural dynamics

Consider a structural domain $\Omega^{\mathrm{s}} \subset \mathbb{R}^2$ with the boundary Γ^{s} which comprises the same three types of boundaries as well. A structure immersed in a fluid continuously sustains the fluctuating fluid force. The equation of motion is expressed in the Lagrangian description with proper initial and boundary conditions. The isotropic assumption is made for the structural problem.

4.1 Rigid–body motion

In the case of a single rigid body undergoing both translation and rotation (see Fig. 4), the structural displacement is represented by $\mathbf{d} = \{d_1,\ d_2,\ \theta\}^{\mathrm{T}}$ where subscripts 1, 2 and θ designates the horizontal, vertical and rotational components defined at the center of gravity G, respectively. The equation of structural motion is formulated by

$$ \begin{bmatrix} m_1 & & \\ & m_2 & \\ & & m_\theta \end{bmatrix} \ddot{\mathbf{d}} + \begin{bmatrix} c_1 & & \\ & c_2 & \\ & & c_\theta \end{bmatrix} \dot{\mathbf{d}} + \begin{bmatrix} k_1 & & \\ & k_2 & \\ & & k_\theta \end{bmatrix} \mathbf{d} = \mathbf{R}, \tag{42} $$

where the dot illuminates the derivative with respect to t, m_i, c_i and k_i ($i = 1,\ 2$ and θ) stand for the generalized mass, damping and stiffness of the structure, $\mathbf{R} = \{F_{\mathrm{d}},\ F_{\mathrm{l}},\ F_{\mathrm{m}}\}^{\mathrm{T}}$ is the applied fluid force, F_{d}, F_{l} and F_{m} signify the drag, lift and pitching moment, respectively. As pictured in Fig. 4, the compatibility condition must be satisfied between the surface point P and the center of gravity G [55].

Next, the dimensionless scales

$$ \hat{\mathbf{x}} = \frac{\mathbf{x}}{L},\ \hat{t} = \frac{tU}{L},\ \hat{d}_1 = \frac{d_1}{L},\ \hat{d}_2 = \frac{d_2}{L}, $$

$$ C_{\mathrm{d}} = \frac{2F_{\mathrm{d}}}{\rho^{\mathrm{f}} U^2 L},\ C_{\mathrm{l}} = \frac{2F_{\mathrm{l}}}{\rho^{\mathrm{f}} U^2 L},\ C_{\mathrm{m}} = \frac{2F_{\mathrm{m}}}{\rho^{\mathrm{f}} U^2 L^2}, $$

$$ \hat{m}_1 = \frac{m_1}{\rho^{\mathrm{f}} L^2},\ \hat{m}_2 = \frac{m_2}{\rho^{\mathrm{f}} L^2},\ \hat{m}_\theta = \frac{m_\theta}{\rho^{\mathrm{f}} L^4} $$

and the reduced parameters

$$ \xi_1 = \frac{c_1}{2\sqrt{m_1 k_1}},\ \xi_2 = \frac{c_2}{2\sqrt{m_2 k_2}},\ \xi_\theta = \frac{c_\theta}{2\sqrt{m_\theta k_\theta}}, $$

$$f_{\mathrm{r}1} = \frac{f_{\mathrm{n}1}L}{U},\ f_{\mathrm{r}2} = \frac{f_{\mathrm{n}2}L}{U},\ f_{\mathrm{r}\theta} = \frac{f_{\mathrm{n}\theta}L}{U},$$

$$f_{\mathrm{n}1} = \frac{1}{2\pi}\sqrt{\frac{k_1}{m_1}},\ f_{\mathrm{n}2} = \frac{1}{2\pi}\sqrt{\frac{k_2}{m_2}},\ f_{\mathrm{n}\theta} = \frac{1}{2\pi}\sqrt{\frac{k_\theta}{m_\theta}}$$

are computed to nondimensionalize Eq. (42), where the drag coefficient C_{d}, the life coefficient C_{l} and the moment coefficient C_{m} are the dimensionless applied forces, the mass ratio $\hat{m}_i$ is the dimensionless mass, ξ_i is the damping ratio, $f_{\mathrm{r}i}$ is the reduced natural frequency, and $f_{\mathrm{n}i}$ is the natural frequency. Therefore, the dimensionless equation of structural motion is visualized as

$$\ddot{\mathbf{d}} + 4\pi \begin{bmatrix} f_{\mathrm{r}1}\xi_1 & & \\ & f_{\mathrm{r}2}\xi_2 & \\ & & f_{\mathrm{r}\theta}\xi_\theta \end{bmatrix} \dot{\mathbf{d}} + 4\pi^2 \begin{bmatrix} (f_{\mathrm{r}1})^2 & & \\ & (f_{\mathrm{r}2})^2 & \\ & & (f_{\mathrm{r}\theta})^2 \end{bmatrix} \mathbf{d} = \begin{Bmatrix} \dfrac{C_{\mathrm{d}}}{2\hat{m}_1} \\ \dfrac{C_{\mathrm{l}}}{2\hat{m}_2} \\ \dfrac{C_{\mathrm{m}}}{2\hat{m}_\theta} \end{Bmatrix}. \quad (43)$$

4.2 Flexible–body motion

For an elastic solid, the elastodynamics equation governing the conservation law of linear momentum reads as

$$\rho^{\mathrm{s}}\left(\ddot{\mathbf{d}} - \mathbf{f}^{\mathrm{s}}\right) - \nabla \cdot \boldsymbol{\sigma}^{\mathrm{s}} = \mathbf{0}, \quad (44)$$

where ρ^{s} is the structural density, $\mathbf{f}^{\mathrm{s}}$ is the structural body force, $\boldsymbol{\sigma}^{\mathrm{s}}$ is the Cauchy stress tensor and the structural damping is omitted. Other material constants contain Young's modulus E and Poisson's ratio ν. The plane stress assumption is made for the two-dimensional case.

To accommodate the geometrical nonlinearity, the Saint Venant–Kirchhoff constitutive model is assumed below

$$\mathbf{S} = \mathbf{D} : \mathbf{E} \quad \text{and} \quad \mathbf{E} = \frac{1}{2}(\mathbf{F}^{\mathrm{T}} \cdot \mathbf{F} - \mathbf{I}), \quad (45)$$

where $\mathbf{S}$ is the second Piola–Kirchhoff stress tensor, $\mathbf{D}$ stands for the constitutive tensor, $\mathbf{E}$ means the Green–Lagrangian strain tensor, and $\mathbf{F} = \mathbf{I} + \nabla\mathbf{d}$ is the deformation gradient tensor. The second Piola–Kirchhoff stress tensor, $\mathbf{S}$, is related to the Cauchy stress tensor, $\boldsymbol{\sigma}^{\mathrm{s}}$, via the geometric transformation given by

$$\mathbf{S} = J\mathbf{F}^{-1}\boldsymbol{\sigma}^{\mathrm{s}}\mathbf{F}^{-\mathrm{T}}, \quad (46)$$

where $J = \det(\mathbf{F})$.

The initial and boundary conditions are imposed to close the system of solid equations in the following manner

$$\mathbf{d}(\mathbf{x},\ 0) = \mathbf{d}^0, \quad \dot{\mathbf{d}}(\mathbf{x},\ 0) = \dot{\mathbf{d}}^0 \quad \text{on} \quad \Omega_0^{\mathrm{s}}, \quad (47a)$$

$$\mathbf{d} = \mathbf{g}^{\mathrm{s}} \quad \text{on} \quad \Gamma_{\mathrm{d}}^{\mathrm{s}}, \quad \boldsymbol{\sigma}^{\mathrm{s}} \cdot \mathbf{n}^{\mathrm{s}} = \mathbf{h}^{\mathrm{s}} \quad \text{on} \quad \Gamma_{\mathrm{n}}^{\mathrm{s}}, \quad (47b)$$

where $\mathbf{n}^{\mathrm{s}}$ is the unit outward normal of $\Gamma_{\mathrm{n}}^{\mathrm{s}}$.

Likewise, the following dimensionless scales are defined

$$\hat{\mathbf{x}} = \frac{\mathbf{x}}{L},\ \hat{t} = \frac{tU}{L},\ \hat{\mathbf{d}} = \frac{\mathbf{d}}{L},\ \hat{E} = \frac{E}{\rho^{\mathrm{f}} U^2},\ \hat{\mathbf{f}}^{\mathrm{s}} = \frac{\mathbf{f}^{\mathrm{s}} L}{U^2},\ \hat{m} = \frac{\rho^{\mathrm{s}}}{\rho^{\mathrm{f}}}$$

in order to enable the nondimensionalization of Eq. (44). Discarding all superscript hats, the dimensionless version of the geometrically nonlinear elastodynamics equation is established as

$$\ddot{\mathbf{d}} - \frac{1}{\hat{m}} \nabla \cdot \boldsymbol{\sigma}^{\mathrm{s}} - \mathbf{f}^{\mathrm{s}} = \mathbf{0}, \tag{48}$$

alongside with the given initial and boundary conditions.

4.3 Finite element discretization

Here we commence spatial discretization for the elastic solid. As usual, the standard Galerkin procedure is used with the finite element approximation to the displacement, velocity and acceleration

$$\mathbf{d} = \mathbf{N}\bar{\mathbf{d}},\ \dot{\mathbf{d}} = \mathbf{N}\dot{\bar{\mathbf{d}}},\ \ddot{\mathbf{d}} = \mathbf{N}\ddot{\bar{\mathbf{d}}}, \tag{49}$$

which generates the incremental equilibrium equation for dynamic analysis below

$$\mathbf{K}^n \Delta\bar{\mathbf{d}} = \mathbf{R}^{n+1} - \mathbf{P}^n - \mathbf{M}^{\mathrm{s}} \ddot{\bar{\mathbf{d}}}^{n+1}, \tag{50}$$

where $\mathbf{K}$ represents the tangent stiffness matrix, $\mathbf{M}^{\mathrm{s}}$ is the mass matrix, $\Delta\bar{\mathbf{d}} = \bar{\mathbf{d}}^{n+1} - \bar{\mathbf{d}}^n$ is the increment of nodal displacement, $\mathbf{R}$ is the external force and $\mathbf{P}$ is the internal force.

Depending upon the geometrical nonlinearity, it is necessary to iterate Eq. (50) in each load step until a required tolerance is satisfied. This linearization is carried out by the modified Newton–Raphson procedure using total Lagrangian formulation [2]. The mass of the body considered is assumed to be conserved in dynamic analysis. Hence the smoothed equilibrium iteration equation is written as

$$\widetilde{\mathbf{K}}^n \delta\bar{\mathbf{d}}^{(k)} = \mathbf{R}^{n+1} - \widetilde{\mathbf{P}}^{n+1(k-1)} - \mathbf{M}^{\mathrm{s}} \ddot{\bar{\mathbf{d}}}^{n+1(k)}, \tag{51}$$

where $\delta\bar{\mathbf{d}}^{(k)}$ is the incremental displacement in the k-th subiteration at the current time step and the tangent stiffness matrix is decomposed into linear and nonlinear parts, namely $\widetilde{\mathbf{K}} = \widetilde{\mathbf{K}}_{\mathrm{l}} + \widetilde{\mathbf{K}}_{\mathrm{nl}}$. The resultant matrices and vectors admit the following representation

$$\Delta\bar{\mathbf{d}}^{(k)} = \Delta\bar{\mathbf{d}}^{(k-1)} + \delta\bar{\mathbf{d}}^{(k)},\ \mathbf{M}^{\mathrm{s}} = \hat{m} \int_{\Omega_0^{\mathrm{s}}} \mathbf{N}^{\mathrm{T}} \mathbf{N} \mathrm{d}\Omega,\ \mathbf{R} = \hat{m} \int_{\Omega^{\mathrm{s}}} \mathbf{N}^{\mathrm{T}} \mathbf{f}^{\mathrm{s}} \mathrm{d}\Omega + \int_{\Gamma_{\mathrm{n}}^{\mathrm{s}}} \mathbf{N}^{\mathrm{T}} \mathbf{h}^{\mathrm{s}} \mathrm{d}\Gamma,$$

$$\widetilde{\mathbf{K}}_{\mathrm{l}} = \int_{\Omega_0^{\mathrm{s}}} \widetilde{\mathbf{B}}_{\mathrm{l}}^{\mathrm{T}} \mathbf{D} \widetilde{\mathbf{B}}_{\mathrm{l}} \mathrm{d}\Omega,\ \widetilde{\mathbf{K}}_{\mathrm{nl}} = \int_{\Omega_0^{\mathrm{s}}} \widetilde{\mathbf{B}}_{\mathrm{nl}}^{\mathrm{T}} \widetilde{\mathbf{S}} \widetilde{\mathbf{B}}_{\mathrm{nl}} \mathrm{d}\Omega,\ \widetilde{\mathbf{P}} = \int_{\Omega^{\mathrm{s}}} \widetilde{\mathbf{B}}_{\mathrm{l}}^{\mathrm{T}} \widetilde{\boldsymbol{\sigma}}^{\mathrm{s}} \mathrm{d}\Omega.$$

The key to compute these quantities consists in the smoothed deformation gradient tensor $\widetilde{\mathbf{F}} = \mathbf{I} + \widetilde{\nabla}\mathbf{d}$ [14,13]. Details of the modified Newton–Raphson procedure considering specific time discretization methods can be found in [2,7].

4.4 Time marching method

The widespread availability of step-by-step time integration algorithms is seen in computational analyses of structural dynamics. Here, the structural movement is integrated in time with the Generalized-α method [11] which is generally superior to the Newmark-β method [52]. To do this, the semi-discrete equation of motion is applied to a general midpoint within one time interval, implying that the following modified equation holds

$$\mathbf{M}^{\mathrm{s}}\ddot{\bar{\mathbf{d}}}^{n+1-\alpha_{\mathrm{m}}}+\mathbf{C}\dot{\bar{\mathbf{d}}}^{n+1-\alpha_{\mathrm{f}}}+\mathbf{K}\bar{\mathbf{d}}^{n+1-\alpha_{\mathrm{f}}}=\mathbf{R}^{n+1-\alpha_{\mathrm{f}}}, \tag{52}$$

where $\mathbf{M}^{\mathrm{s}}$, $\mathbf{C}$ and $\mathbf{K}$ represent the mass, damping and stiffness matrices, respectively, and we prescribe

$$\ddot{\bar{\mathbf{d}}}^{n+1-\alpha_{\mathrm{m}}}=(1-\alpha_{\mathrm{m}})\ddot{\bar{\mathbf{d}}}^{n+1}+\alpha_{\mathrm{m}}\ddot{\bar{\mathbf{d}}}^{n}, \tag{53a}$$

$$\dot{\bar{\mathbf{d}}}^{n+1-\alpha_{\mathrm{f}}}=(1-\alpha_{\mathrm{f}})\dot{\bar{\mathbf{d}}}^{n+1}+\alpha_{\mathrm{f}}\dot{\bar{\mathbf{d}}}^{n}, \tag{53b}$$

$$\bar{\mathbf{d}}^{n+1-\alpha_{\mathrm{f}}}=(1-\alpha_{\mathrm{f}})\bar{\mathbf{d}}^{n+1}+\alpha_{\mathrm{f}}\bar{\mathbf{d}}^{n}, \tag{53c}$$

$$\mathbf{R}^{n+1-\alpha_{\mathrm{f}}}=(1-\alpha_{\mathrm{f}})\mathbf{R}^{n+1}+\alpha_{\mathrm{f}}\mathbf{R}^{n}. \tag{53d}$$

To set $\bar{\mathbf{d}}^{n+1}$ as the single unknowns in Eq. (52), the Newmark approximations [52] to the acceleration and velocity at t^{n+1} are stated as

$$\ddot{\bar{\mathbf{d}}}^{n+1}=\frac{1}{\beta\Delta t^2}(\bar{\mathbf{d}}^{n+1}-\bar{\mathbf{d}}^{n})-\frac{1}{\beta\Delta t}\dot{\bar{\mathbf{d}}}^{n}-\frac{1-2\beta}{2\beta}\ddot{\bar{\mathbf{d}}}^{n}, \tag{54}$$

$$\dot{\bar{\mathbf{d}}}^{n+1}=\frac{\gamma}{\beta\Delta t}(\bar{\mathbf{d}}^{n+1}-\bar{\mathbf{d}}^{n})-\frac{\gamma-\beta}{\beta}\dot{\bar{\mathbf{d}}}^{n}-\frac{\gamma-2\beta}{2\beta}\Delta t\ddot{\bar{\mathbf{d}}}^{n}. \tag{55}$$

Accordingly, the generalized midpoint acceleration and velocity are given by

$$\ddot{\bar{\mathbf{d}}}^{n+1-\alpha_{\mathrm{m}}}=\frac{1-\alpha_{\mathrm{m}}}{\beta\Delta t^2}(\bar{\mathbf{d}}^{n+1}-\bar{\mathbf{d}}^{n})-\frac{1-\alpha_{\mathrm{m}}}{\beta\Delta t}\dot{\bar{\mathbf{d}}}^{n}-\frac{1-\alpha_{\mathrm{m}}-2\beta}{2\beta}\ddot{\bar{\mathbf{d}}}^{n}, \tag{56}$$

$$\dot{\bar{\mathbf{d}}}^{n+1-\alpha_{\mathrm{f}}}=\frac{(1-\alpha_{\mathrm{f}})\gamma}{\beta\Delta t}(\bar{\mathbf{d}}^{n+1}-\bar{\mathbf{d}}^{n})-\frac{(1-\alpha_{\mathrm{f}})\gamma-\beta}{\beta}\dot{\bar{\mathbf{d}}}^{n}-\frac{(\gamma-2\beta)(1-\alpha_{\mathrm{f}})}{2\beta}\Delta t\ddot{\bar{\mathbf{d}}}^{n}. \tag{57}$$

The time integration parameters β, γ, α_{m} and α_{f} are defined as functions of the spectral radius ρ_∞ [11], whose optimal expressions take the form of

$$\beta=\frac{1}{4}(1-\alpha_{\mathrm{m}}+\alpha_{\mathrm{f}})^2,\ \gamma=\frac{1}{2}-\alpha_{\mathrm{m}}+\alpha_{\mathrm{f}},\ \alpha_{\mathrm{m}}=\frac{2\rho_\infty-1}{\rho_\infty+1},\ \alpha_{\mathrm{f}}=\frac{\rho_\infty}{\rho_\infty+1}, \tag{58}$$

where $0\leqslant\rho_\infty\leqslant 1$ for the desired level of numerical dissipation. Here we specify $\rho_\infty=0.1$ for the rigid body [16] whereas $\rho_\infty=0.5$ for the elastic solid [17].

In addition, the calculation of smoothed internal force complies with the interpretation of [43]

$$\widetilde{\mathbf{P}}^{n+1-\alpha_{\mathrm{f}}}=(1-\alpha_{\mathrm{f}})\widetilde{\mathbf{P}}^{n+1}+\alpha_{\mathrm{f}}\widetilde{\mathbf{P}}^{n}=(1-\alpha_{\mathrm{f}})\widetilde{\mathbf{P}}(\mathbf{d}^{n+1})+\alpha_{\mathrm{f}}\widetilde{\mathbf{P}}(\mathbf{d}^{n}), \tag{59}$$

while working on the elastic solid.

5 Two-level mesh updating

Imposition of interface conditions in time requires that the position of moving interface is accurately captured in the ALE domain whilst maintaining the satisfactory mesh quality. Hence the mesh deformation is of cardinal significance in fluid–structure coupling. For instance, in the space-time FEM the variational formulation written over its space-time domain automatically takes into account the deformation of the spatial domain with respect to time. Such a process is particularly effective for forced motion of a cylinder where the mesh movement is known *a priori* [64]. For free motion of a body, a general pseudo-elasticity equation approach is proposed in association with the stabilized space-time FEM [39].

The present mesh deformation method adopts a blend of moving submesh approach (MSA) [45] and the ortho-semi-torsional spring analogy model [51] in the ALE context. Its fundamental principle comprises two stages below

- Spring analogy method assimilates the triangle submesh to the structural motion;
- MSA creates a mapping between the submesh's deformation and that of ALE mesh.

Interested readers are recommended to refer to [32,33,24,31] for thorough implementation. Though MSA moves fluid nodes with the aid of a background mesh, this technique can reduce the expenditure on spring analogy method while preserving the mesh topology [33,30].

On the other hand, the midpoint rule is applied to the mesh velocity scheme as it automatically meets geometric conservation law for two-dimensional stabilized FEM [46] and outstrips the second-order differencing scheme [19].

6 Partitioned solution strategy

6.1 Interface coupling conditions

In the partitioned scheme, the interplay between the fluid and structure is accomplished via separately enforcing the velocity continuity and traction equilibrium on Σ as follows

$$\mathbf{u} = \dot{\mathbf{d}} \quad \text{and} \quad \mathbf{t}^{\mathrm{f}} = \mathbf{t}^{\mathrm{s}}, \tag{60}$$

where $\mathbf{t}^{\mathrm{f}} = \boldsymbol{\sigma}^{\mathrm{f}} \cdot \mathbf{n}^{\mathrm{s}}$ and $\mathbf{t}^{\mathrm{s}} = \boldsymbol{\sigma}^{\mathrm{s}} \cdot \mathbf{n}^{\mathrm{s}}$ are the fluid and structural tractions, respectively, $\mathbf{n}^{\mathrm{s}}$ represents the unit outward normal of Σ pointing from the structure to the fluid and $\mathbf{n}^{\mathrm{f}} = -\mathbf{n}^{\mathrm{s}}$. Since the external force acting on the immersed rigid body is a concentrated load vector, the stress equilibrium on Σ becomes

$$\int_{\Sigma} \mathbf{t}^{\mathrm{f}} \mathrm{d}\Gamma = \int_{\Sigma} \mathbf{t}^{\mathrm{s}} \mathrm{d}\Gamma \quad \text{and} \quad \int_{\Sigma} \Delta\mathbf{x} \times \mathbf{t}^{\mathrm{f}} \mathrm{d}\Gamma = \int_{\Sigma} \Delta\mathbf{x} \times \mathbf{t}^{\mathrm{s}} \mathrm{d}\Gamma, \tag{61}$$

where $\Delta\mathbf{x}$ is the distance between surface point P and center of gravity G, as shown in Fig. 4. Also, the geometrical continuity is supplemented thanks to the mesh movement

$$\mathbf{x} = \mathbf{d} \quad \text{and} \quad \mathbf{w} = \dot{\mathbf{d}}. \tag{62}$$

Moreover, interface conditions (60)–(62) may be recast in a hybrid way to alleviate the adverse time-lag effect [36,29,30].

6.2 Block-Gauss–Seidel coupling algorithm

The FSI system constitutes a coupled set of nonlinear algebraic equations to be solved for each time step. For numerical stability, kinematic and kinetic compatibilities are compulsively imposed on Σ through block-Gauss–Seidel procedure which implicitly couples all interacting fields. Extra acceleration technique like the Aitken's Δ^2 method [44] may be adopted for faster convergence. Within one time interval, the present coupling algorithm is elaborated hereinafter.

Step 1: Initialize all variables and set $k = 0$
Step 2: Extrapolate the interface

$$\bar{\mathbf{x}}_{\Sigma}^{n+1(k)} = \mathbf{d}_{\Sigma}^{n} + \left(\frac{3}{2}\dot{\mathbf{d}}_{\Sigma}^{n} - \frac{1}{2}\dot{\mathbf{d}}_{\Sigma}^{n-1}\right)\Delta t$$

Step 3: Start fixed-point iterations and set $k \leftarrow k + 1$
Step 4: Rearrange the fluid mesh $\Omega_{n+1(k)}^{\mathrm{f}}$
Step 5: Calculate the mesh velocity

$$\mathbf{w}^{n+1(k)} = \frac{\bar{\mathbf{x}}^{n+1(k)} - \mathbf{x}^{n}}{\Delta t}$$

Step 6: Derive other geometrical quantities if necessary
Step 7: Compute the intermediate velocity

$$\mathbf{u}^{*} - \mathbf{u}^{n} = \Delta t\left(-\mathbf{c}^{n}\cdot\widetilde{\nabla}\mathbf{u}^{n} - \widetilde{\nabla}p^{n} + \frac{1}{Re}\widetilde{\nabla}^{2}\mathbf{u}^{n} + \frac{\Delta t}{2}\mathbf{c}^{n}\cdot\widetilde{\nabla}(\mathbf{c}^{n}\cdot\widetilde{\nabla}\mathbf{u}^{n} + \widetilde{\nabla}p^{n})\right)$$

Step 8: Update the pressure

$$\widetilde{\nabla}^{2}p^{n+1(k)} = \frac{1}{\Delta t + \phi}\left(\widetilde{\nabla}\cdot\mathbf{u}^{*} + \Delta t\widetilde{\nabla}^{2}p^{n} + \phi\widetilde{\nabla}\cdot\mathbf{q}^{n}\right)$$

Step 9: Correct the velocity

$$\mathbf{u}^{n+1(k)} - \mathbf{u}^{*} = -\Delta t\left(\widetilde{\nabla}(p^{n+1(k)} - p^{n}) - \frac{\Delta t}{2}\mathbf{c}^{n}\cdot\widetilde{\nabla}^{2}(p^{n+1(k)} - p^{n})\right)$$

Step 10: Renew the auxiliary variable

$$\mathbf{q}^{n+1(k)} = \widetilde{\nabla}p^{n+1(k)}$$

Step 11: Deduce the fluid load and pass it to the structure/solid
Step 12: Solve equation of the structural equation

$$\left(\frac{1-\alpha_{\mathrm{m}}}{\beta\Delta t^{2}}\mathbf{M}^{\mathrm{s}} + \frac{(1-\alpha_{\mathrm{f}})\gamma}{\beta\Delta t}\mathbf{C} + (1-\alpha_{\mathrm{f}})\mathbf{K}\right)\mathbf{d}^{n+1(k)} =$$
$$(1-\alpha_{\mathrm{f}})\mathbf{R}^{n+1(k)} + \alpha_{\mathrm{f}}\mathbf{R}^{n} + \mathbf{M}^{\mathrm{s}}\left(\frac{1-\alpha_{\mathrm{m}}}{\beta\Delta t^{2}}\mathbf{d}^{n} + \frac{1-\alpha_{\mathrm{m}}}{\beta\Delta t}\dot{\mathbf{d}}^{n} + \frac{1-\alpha_{\mathrm{m}}-2\beta}{2\beta}\ddot{\mathbf{d}}^{n}\right) +$$
$$\mathbf{C}\left(\frac{(1-\alpha_{\mathrm{f}})\gamma}{\beta\Delta t}\mathbf{d}^{n} + \frac{(1-\alpha_{\mathrm{f}})\gamma-\beta}{\beta}\dot{\mathbf{d}}^{n} + \frac{(1-\alpha_{\mathrm{f}})(\gamma-2\beta)}{2\beta}\Delta t\ddot{\mathbf{d}}^{n}\right) - \alpha_{\mathrm{f}}\mathbf{K}\mathbf{d}^{n}$$

Step 13: Estimate the interfacial residuals

$$\mathbf{g}^{n+1(k)} = \mathbf{x}_{\Sigma}^{n+1(k)} - \bar{\mathbf{x}}_{\Sigma}^{n+1(k-1)}$$

Step 14: Check the convergence and the maximum number of subiterations: if not convergent, then go ahead; otherwise, proceed to the next time step

Step 15: Relax the position of the interface

$$\bar{\mathbf{x}}_{\Sigma}^{n+1(k)} = \omega \mathbf{x}_{\Sigma}^{n+1(k)} + (1-\omega)\bar{\mathbf{x}}_{\Sigma}^{n+1(k-1)}$$

Step 16: Return to **Step 3**

The stop criterion at the k-th subiteration is simply judged with

$$\max(\mathbf{g}_1^{n(k)},\ \mathbf{g}_2^{n(k)},\ \mathbf{g}_3^{n(k)},\ \cdots,\ \mathbf{g}_{n_{\mathrm{fs}}}^{n(k)}) < \varepsilon \quad \text{and} \quad k < k_{\max}, \tag{63}$$

where n_{fs} is the number of nodes on the interface, the convergence tolerance is $\varepsilon = 1.0 \times 10^{-6}$ and $k_{\max} = 200$ is the user-defined constant that controls the maximum subiterations at each time step.

Alternatively, a variant algorithm may be acquired in case that Eq. (18) is discretized in time by

$$\widetilde{\nabla} \cdot \mathbf{u}^{n+1(k)} + \phi \widetilde{\nabla} \cdot \mathbf{q}^{n+1(k-1)} - \phi \widetilde{\nabla}^2 p^{n+1(k)} = 0. \tag{64}$$

7 Results and discussion

7.1 Steady cavity flow

The geometry of lid-driven cavity flow is defined in Fig. 5(a). The cavity is meshed with 40×40 Q4 elements in Fig. 5(b). $Re = 100$ and $\Delta t = 1.0 \times 10^{-2}$ are chosen for this problem. The velocity components computed without the SPGP technique are severely oscillatory in Fig. 6. This is because the pressure difference $p^{n+1} - p^n$ will approach to zero in the CBS scheme once steady state is reached. Furthermore, in accordance with [12,1], the stability of the second-order scheme seems more sensitive to a smaller time step.

Fig. 7 exhibits no oscillations at steady state since the difference between the Laplacian of p and the divergence of $\mathbf{q}$ multiplied by ϕ stabilizes the pressure variation. Besides, the curve obtained from a smaller ϕ is closer to [21]. Nithiarasu and Zienkiewicz [54] explained that modifying ϕ possibly reduces numerical oscillations but could incur accuracy deterioration elsewhere. Among all ϕ in Table 1, $\phi = 0.25\Delta t$ demands the least run time on a laptop with Intel(R) core(TM) i5-5200U CPU and 16GB RAM. Therefore, ϕ may affect the numerical expense of large-scale computations.

7.2 Unsteady flow over a circular cylinder

The incompressible flow past a circular cylinder is attempted at $Re = 100$. The problem definition is plotted in Fig. 8(a) whereas the finite element discretization is composed of 5190 Q4 elements and 5341 nodes in Fig. 8(b). The time step is set as $\Delta t = 1.0 \times 10^{-2}$.

Table 2 lists the mean value of drag coefficient $C_{\mathrm{d,mean}}$, the root-mean-square error (RMSE) of drag coefficient $C_{\mathrm{d,rmse}}$, the amplitude of lift coefficient $C_{\mathrm{l,max}}$, the RMSE of lift coefficient $C_{\mathrm{l,rmse}}$ and the Strouhal number St. The unstabilized

scheme generates larger values of the first three indicators, whereas all stabilized schemes agree well with the existing data [22, 66, 5, 42, 56, 32, 6]. The predicted time-varying C_{d} and C_{l} underline the negligible deviation between $\phi = 0.1\Delta t$ and $1.0\Delta t$ in Fig. 9. The expenditure examined in Table 3 explains that $\phi = 0.25\Delta t$ consumes the least time again. Unlike the steady flow, adjusting ϕ does not deteriorate the accuracy. In Fig. 10, the vorticity contour using $\phi = 0.25\Delta t$ reflects that a repeating pattern of swirling vortices is caused by unsteady separation of the flow around the blunt body.

7.3 Vortex-induced vibration of a very light circular cylinder

Fig. 11 graphically illustrates free oscillations of a circular cylinder. System parameters are given as [37]: $f_{\mathrm{r}} = 0.2$, $\xi = 0$, $Re = 100$ and $\hat{m} = 0.471$ to $\hat{m} = 0.157$. For numerical efficiency, the computational domain is divided into the Eulerian, ALE and Lagrangian subdomains. The finite element mesh comprising 8880 Q4 elements and 9090 nodes, and the corresponding submesh are demonstrated in Fig. 12. The time step is $\Delta t = 1.0 \times 10^{-2}$ and the relaxation factor is $\omega = 0.5$.

Table 4 analyzes the ϕ-sensitivity through the $\hat{m} = 0.471$ case. We see that the unstabilized scheme begets a failure whereas the stabilized schemes give nearly identical data. We choose $\phi = 1.0\Delta t$ for all mass ratios, given its performance. Eq. (33) still holds for FSI as the stability criterion because $\phi = 1.0\Delta t < \Delta t_{\mathrm{crit}} = 0.2828$.

The time history of aerodynamic parameters is plotted in Fig. 13 for $\hat{m} = 0.408$, at which our FSI method establishes the stable and smooth cylinder response. However, the enlarged view in Fig. 14(a) indicates the failure of the traditional strong staggered coupling (SSC) scheme [37]. By contrast, the present coupling scheme based upon standard fixed-point iterations agrees well with that computed by the nonlinear interface force correction (NFIC) approach [37].

Fig. 15 shows the x_1-x_2 trajectory at various $\hat{m}$, illustrating that the VIV at low Re is a self-limiting process [76]. The cylinder takes on the nearly symmetrical trajectory shaping the classical *Lissajous* figure of "8". Vorticity fields at $\hat{m} = 0.393$, 0.298 and 0.157 are displayed in Fig. 16 where the 2S vortex-shedding mode [69] is seen in the wake.

7.4 Vortex-induced vibration of a flexible beam behind an obstacle

The benchmark problem proposed by Wall and Ramm [67] is schematically demonstrated in Fig. 17. Physical parameters are specified as: $\rho^{\mathrm{f}} = 1.18 \times 10^{-3}$, $\mu = 1.82 \times 10^{-4}$, $\rho^{\mathrm{s}} = 1.0 \times 10^{-1}$, $E = 2.5 \times 10^{6}$, $\nu = 0.35$, $L = 1$, $U = 51.3$ and $Re = 332.6$. The meshing information is listed in Table 5. The fluid mesh and MSA submesh are exhibited in Fig. 18. $\Delta t = 1.0 \times 10^{-2}$ and $\omega = 0.9$ are utilized here.

The almost equal results are reported in Table 6 among different ϕ, but $\phi = 0$ incurs slow convergence at initial stage. As before, we adopt $\phi = 1.0\Delta t$ here. Table 7 summarizes d_{max2} and f_{o} documented in the open literature [67, 61, 17, 47, 3, 7, 41, 23, 15, 20, 25, 28, 40]. The obtained results are in good agreement with the

available data. Note that $f_o = 0.0582$ is very close to the first eigenfrequency of the beam, $f_1^s = 0.0591$, which predominates the structural oscillations.

The unsteady periodic long-term oscillatory vibration of the tip is fairly depicted in Fig. 19(a). Fig. 19(b) demonstrates that the slightly longer time is required to reach the smaller characteristic amplitude in [28]. However, the underestimated amplitude may be obtained even though denser spatial discretization or higher-order interpolation is used for the beam [41, 15, 20, 40]. Three typical snapshots of vorticity and pressure fields are displayed in Fig. 20. It is seen that transient flow patterns and structural oscillations vary significantly in different phases.

8 Conclusions

This paper has reported the straightforward implementation of CS-FEM into two major areas of CFD. The stabilized second-order S-CBS scheme is proposed to solve incompressible NS equations. In the fluid equations GPs cooperates with equal SCs for each smoothed element integral, whereas CS-FEM works for the solid routinely. The structural equations are advanced in time by the Generalized-α method. The dynamic mesh is efficiently updated via MSA in combination with spring analogy method. Block-Gauss–Seidel procedure is adopted for the fluid–structure interplay within the ALE framework. The proposed methodologies do not only make trivial revision to available FE codes, but also exhibit outstanding performance in numerical tests. The main findings are summarized below

- The SPGP technique is crucial to the second-order S-CBS scheme in incompressible flows and FSI.
- The stabilization parameter has an impact on numerical accuracy and efficiency. In particular, Eq. (34) is recommended for the Eulerian flows while Eq. (33) for FSI.
- The FSI solver never asks for accelerated fixed-point iterations even in the case of extremely low mass ratio.

Acknowledgements Support from National Natural Science Foundation of China under grant number 51508332 is gratefully acknowledged.

References

1. Bao, Y., Zhou, D., Huang, C.: Numerical simulation of flow over three circular cylinders in equilateral arrangements at low Reynolds number by a second-order characteristic-based split finite element method. Computers & Fluids **39**(5), 882–899 (2010)
2. Bathe, K.J., Ramm, E., Wilson, E.L.: Finite element formulations for large deformation dynamic analysis. International Journal for Numerical Methods in Engineering **9**(2), 353–386 (1975)
3. Bazilevs, Y., Calo, V.M., Hughes, T.J.R., Zhang, Y.: Isogeometric fluid–structure interaction: theory, algorithms, and computations. Computational Mechanics **43**(1), 3–37 (2008)
4. Bazilevs, Y., Takizawa, K., Tezduyar, T.E.: Computational Fluid–Structure Interaction: Methods and Applications. John Wiley & Sons, Chichester, West Sussex, UK (2013)
5. Behr, M., Hastreiter, D., Mittal, S., Tezduyar, T.E.: Incompressible flow past a circular cylinder: dependence of the computed flow field on the location of the lateral boundaries. Computer Methods in Applied Mechanics and Engineering **123**(1-4), 309–316 (1995)

6. Bevan, R.L.T., Boileau, E., van Loon, R., Lewis, R.W., Nithiarasu, P.: A comparative study of fractional step method in its quasi-implicit, semi-implicit and fully-explicit forms for incompressible flows. International Journal of Numerical Methods for Heat & Fluid Flow **26**(3/4), 595–623 (2016)
7. Braun, A.L., Awruch, A.M.: A partitioned model for fluid–structure interaction problems using hexahedral finite elements with one-point quadrature. International Journal for Numerical Methods in Engineering **79**(5), 505–549 (2009)
8. Brooks, A.N., Hughes, T.J.R.: Streamline upwind/Petrov-Galerkin formulations for convection dominated flows with particular emphasis on the incompressible Navier–Stokes equations. Computer Methods in Applied Mechanics and Engineering **32**(1-3), 199–259 (1982)
9. Chen, J.S., Wu, C.T., Yoon, S., You, Y.: A stabilized conforming nodal integration for Galerkin mesh-free methods. International Journal for Numerical Methods in Engineering **50**(2), 435–466 (2001)
10. Chorin, A.J.: Numerical solution of the Navier–Stokes equations. Mathematics of Computation **22**(104), 745–762 (1968)
11. Chung, J., Hulbert, G.M.: A time integration algorithm for structural dynamics with improved numerical dissipation: The Generalized-α method. Journal of Applied Mechanics–ASME **60**(2), 371–375 (1993)
12. Codina, R.: Pressure stability in fractional step finite element methods for incompressible flows. Journal of Computational Physics **170**(1), 112–140 (2001)
13. Cui, X.Y., Liu, G.R., Li, G.Y., Zhao, X., Nguyen, T.T., Sun, G.Y.: A smoothed finite element method (SFEM) for linear and geometrically nonlinear analysis of plates and shells. CMES: Computer Modeling in Engineering & Sciences **28**(2), 109–126 (2008)
14. Dai, K.Y., Liu, G.R.: Free and forced vibration analysis using the smoothed finite element method (SFEM). Journal of Sound and Vibration **301**(3), 803–820 (2007)
15. De Rosis, A., Falcucci, G., Ubertini, S., Ubertini, F.: A coupled lattice Boltzmann-finite element approach for two-dimensional fluid–structure interaction. Computers & Fluids **86**, 558–568 (2013)
16. Dettmer, W., Perić, D.: A computational framework for fluid–rigid body interaction: Finite element formulation and applications. Computer Methods in Applied Mechanics and Engineering **195**(13), 1633–1666 (2006)
17. Dettmer, W., Perić, D.: A computational framework for fluid–structure interaction: Finite element formulation and applications. Computer Methods in Applied Mechanics and Engineering **195**(41-43), 5754–5779 (2006)
18. Donea, J.: A Taylor–Galerkin method for convective transport problems. International Journal for Numerical Methods in Engineering **20**(1), 101–119 (1984)
19. Förster, C., Wall, W.A., Ramm, E.: Artificial added mass instabilities in sequential staggered coupling of nonlinear structures and incompressible viscous flows. Computer Methods in Applied Mechanics and Engineering **196**(7), 1278–1293 (2007)
20. Froehle, B., Persson, P.O.: A high-order discontinuous Galerkin method for fluid–structure interaction with efficient implicit-explicit time stepping. Journal of Computational Physics **272**(9), 455–470 (2014)
21. Ghia, U., Ghia, K.N., Shin, C.T.: High-Re solutions for incompressible flow using the Navier–Stokes equations and a multigrid method. Journal of Computational Physics **48**(3), 387–411 (1982)
22. Graham, J.M.R.: Report on the session comparing computation of flow past circular cylinders with experimental data. In: IUTAM Symposium: Bluff-Body Wakes, Dynamics and Instabilities, pp. 317–323. Springer Berlin Heidelberg, Göttingen, Germany (1992)
23. Habchi, C., Russeil, S., Bougeard, D., Harion, J.L., Lemenand, T., Ghanem, A., Valle, D.D., Peerhossaini, H.: Partitioned solver for strongly coupled fluid–structure interaction. Computers & Fluids **71**, 306–319 (2013)
24. He, T.: On a partitioned strong coupling algorithm for modeling fluid–structure interaction. International Journal of Applied Mechanics **7**(2), 1550,021 (2015)
25. He, T.: Partitioned coupling strategies for fluid–structure interaction with large displacement: Explicit, implicit and semi-implicit schemes. Wind & Structures **20**(3), 423–448 (2015)
26. He, T.: A partitioned implicit coupling strategy for incompressible flow past an oscillating cylinder. International Journal of Computational Methods **12**(2), 1550,012 (2015)
27. He, T.: Semi-implicit coupling of CS-FEM and FEM for the interaction between a geometrically nonlinear solid and an incompressible fluid. International Journal of Computational Methods **12**(5), 1550,025 (2015)

28. He, T.: A CBS-based partitioned semi-implicit coupling algorithm for fluid–structure interaction using MCIBC method. Computer Methods in Applied Mechanics and Engineering **298**, 252–278 (2016)
29. He, T., Zhang, K.: Combined interface boundary condition method for fluid–structure interaction: Some improvements and extensions. Ocean Engineering **109**, 243–255 (2015)
30. He, T., Zhang, K.: An overview of the combined interface boundary condition method for fluid–structure interaction. Archives of Computational Methods in Engineering **24**(4), 891–934 (2017)
31. He, T., Zhang, K., Wang, T.: AC-CBS-based partitioned semi-implicit coupling algorithm for fluid–structure interaction using stabilized second-order pressure scheme. Communications in Computational Physics **21**(5), 1449–1474 (2017)
32. He, T., Zhou, D., Bao, Y.: Combined interface boundary condition method for fluid–rigid body interaction. Computer Methods in Applied Mechanics and Engineering **223**, 81–102 (2012)
33. He, T., Zhou, D., Han, Z., Tu, J., Ma, J.: Partitioned subiterative coupling schemes for aeroelasticity using combined interface boundary condition method. International Journal of Computational Fluid Dynamics **28**(6-10), 272–300 (2014)
34. Hirt, C.W., Amsden, A.A., Cook, J.L.: An arbitrary Lagrangian–Eulerian computing method for all flow speeds. Journal of Computational Physics **14**(3), 227–253 (1974)
35. Hughes, T.J.R., Franca, L.P., Hulbert, G.M.: A new finite element formulation for computational fluid dynamics: VIII. The Galerkin/least-squares method for advective-diffusive equations. Computer Methods in Applied Mechanics and Engineering **73**(2), 173–189 (1989)
36. Jaiman, R., Geubelle, P., Loth, E., Jiao, X.: Combined interface boundary condition method for unsteady fluid-structure interaction. Computer Methods in Applied Mechanics and Engineering **200**(1), 27–39 (2011)
37. Jaiman, R.K., Pillalamarri, N.R., Guan, M.Z.: A stable second-order partitioned iterative scheme for freely vibrating low-mass bluff bodies in a uniform flow. Computer Methods in Applied Mechanics and Engineering **301**, 187–215 (2016)
38. Jiang, C., Zhang, Z.Q., Han, X., Liu, G.R., Lin, T.: A cell-based smoothed finite element method with semi-implicit CBS procedures for incompressible laminar viscous flows. International Journal for Numerical Methods in Fluids **86**(1), 20–45 (2018)
39. Johnson, A.A., Tezduyar, T.E.: Mesh update strategies in parallel finite element computations of flow problems with moving boundaries and interfaces. Computer Methods in Applied Mechanics and Engineering **119**(1), 73–94 (1994)
40. Kaneko, S., Hong, G., Mitsume, N., Yamada, T., Yoshimura, S.: Partitioned-coupling FSI analysis with active control. Computational Mechanics **60**(4), 549–558 (2017)
41. Kassiotis, C., Ibrahimbegovic, A., Niekamp, R., Matthies, H.G.: Nonlinear fluid–structure interaction problem. Part I: implicit partitioned algorithm, nonlinear stability proof and validation examples. Computational Mechanics **47**(3), 305–323 (2011)
42. Kjellgren, P.: A semi-implicit fractional step finite element method for viscous incompressible flows. Computational Mechanics **20**(6), 541–550 (1997)
43. Kuhl, D., Crisfield, M.A.: Energy-conserving and decaying algorithms in non-linear structural dynamics. International Journal for Numerical Methods in Engineering **45**(5), 569–599 (1999)
44. Küttler, U., Wall, W.A.: Fixed-point fluid–structure interaction solvers with dynamic relaxation. Computational Mechanics **43**(1), 61–72 (2008)
45. Lefrançois, E.: A simple mesh deformation technique for fluid–structure interaction based on a submesh approach. International Journal for Numerical Methods in Engineering **75**(9), 1085–1101 (2008)
46. Lesoinne, M., Farhat, C.: Geometric conservation laws for flow problems with moving boundaries and deformable meshes, and their impact on aeroelastic computations. Computer Methods in Applied Mechanics and Engineering **134**(1), 71–90 (1996)
47. Liew, K.M., Wang, W.Q., Zhang, L.X., He, X.Q.: A computational approach for predicting the hydroelasticity of flexible structures based on the pressure Poisson equation. International Journal for Numerical Methods in Engineering **72**(13), 1560–1583 (2007)
48. Liu, G.R., Dai, K.Y., Nguyen, T.T.: A smoothed finite element method for mechanics problems. Computational Mechanics **39**(6), 859–877 (2007)
49. Liu, G.R., Nguyen, T.T.: Smoothed Finite Element Methods. CRC Press, Boca Raton, Florida, USA (2010)

50. Löhner, R., Morgan, K., Zienkiewicz, O.C.: The solution of non-linear hyperbolic equation systems by the finite element method. International Journal for Numerical Methods in Fluids **4**(11), 1043–1063 (1984)
51. Markou, G.A., Mouroutis, Z.S., Charmpis, D.C., Papadrakakis, M.: The ortho-semi-torsional (OST) spring analogy method for 3D mesh moving boundary problems. Computer Methods in Applied Mechanics and Engineering **196**(4), 747–765 (2007)
52. Newmark, N.M.: A method of computation for structural dynamics. Journal of Engineering Mechanics–ASCE **85**(3), 67–94 (1959)
53. Nithiarasu, P., Codina, R., Zienkiewicz, O.C.: The Characteristic-Based Split (CBS) scheme–a unified approach to fluid dynamics. International Journal for Numerical Methods in Engineering **66**(10), 1514–1546 (2006)
54. Nithiarasu, P., Zienkiewicz, O.C.: Analysis of an explicit and matrix free fractional step method for incompressible flows. Computer Methods in Applied Mechanics and Engineering **195**(41), 5537–5551 (2006)
55. Nomura, T., Hughes, T.J.R.: An arbitrary Lagrangian–Eulerian finite element method for interaction of fluid and a rigid body. Computer Methods in Applied Mechanics and Engineering **95**(1), 115–138 (1992)
56. Norberg, C.: Fluctuating lift on a circular cylinder: review and new measurements. Journal of Fluids and Structures **17**(1), 57–96 (2003)
57. Otoguro, Y., Takizawa, K., Tezduyar, T.E.: Space–time VMS computational flow analysis with isogeometric discretization and a general-purpose NURBS mesh generation method. Computers & Fluids **158**, 189–200 (2017)
58. Takizawa, K., Moorman, C., Wright, S., Christopher, J., Tezduyar, T.E.: Wall shear stress calculations in space–time finite element computation of arterial fluid–structure interactions. Computational Mechanics **46**(1), 31–41 (2010)
59. Takizawa, K., Tezduyar, T.E., Asada, S., Kuraishi, T.: Space–time method for flow computations with slip interfaces and topology changes (ST-SI-TC). Computers & Fluids **141**, 124–134 (2016)
60. Takizawa, K., Tezduyar, T.E., Otoguro, Y., Terahara, T., Kuraishi, T., Hattori, H.: Turbocharger flow computations with the space–time isogeometric analysis (ST-IGA). Computers & Fluids **142**, 15–20 (2017)
61. Teixeira, P.R.F., Awruch, A.M.: Numerical simulation of fluid–structure interaction using the finite element method. Computers & Fluids **34**(2), 249–273 (2005)
62. Témam, R.: Une méthode d'approximation de la solution des équations de Navier–Stokes. Bulletin de la Société Mathématique de France **96**, 115–152 (1968)
63. Tezduyar, T.E.: Stabilized finite element formulations for incompressible flow computations. Advances in Applied Mechanics **28**, 1–44 (1992)
64. Tezduyar, T.E., Behr, M., Liou, J.: A new strategy for finite element computations involving moving boundaries and interfaces–The deforming-spatial-domain/space-time procedure: I. The concept and the preliminary numerical tests. Computer Methods in Applied Mechanics and Engineering **94**(3), 339–351 (1992)
65. Tezduyar, T.E., Behr, M., Mittal, S., Liou, J.: A new strategy for finite element computations involving moving boundaries and interfaces–The deforming-spatial-domain/space-time procedure: II. Computation of free-surface flows, two-liquid flows, and flows with drifting cylinders. Computer Methods in Applied Mechanics and Engineering **94**(3), 353–371 (1992)
66. Tezduyar, T.E., Mittal, S., Ray, S.E., Shih, R.: Incompressible flow computations with stabilized bilinear and linear equal-order-interpolation velocity-pressure elements. Computer Methods in Applied Mechanics and Engineering **95**(2), 221–242 (1992)
67. Wall, W.A., Ramm, E.: Fluid–structure interaction based upon a stabilized (ALE) finite element method. In: S.R. Idelsohn, E. Oñate, E. Dvorkin (eds.) Proceedings of the 4th World Congress on Computational Mechanics: New Trends and Applications, pp. 1–20. CIMNE, Barcelona, Spain (1998)
68. Wang, S., Khoo, B.C., Liu, G.R., Xu, G.X., Chen, L.: Coupling GSM/ALE with ES-FEM-T3 for fluid–deformable structure interactions. Journal of Computational Physics **276**, 315–340 (2014)
69. Williamson, C.H.K., Roshko, A.: Vortex formation in the wake of an oscillating cylinder. Journal of Fluids and Structures **2**(4), 355–381 (1988)
70. Yao, J., Liu, G.R., Narmoneva, D.A., Hinton, R.B., Zhang, Z.Q.: Immersed smoothed finite element method for fluid–structure interaction simulation of aortic valves. Computational Mechanics **90**(6), 1292–1320 (2012)

71. Yoo, J.W., Moran, B., Chen, J.S.: Stabilized conforming nodal integration in the natural-element method. International Journal for Numerical Methods in Engineering **60**(5), 861–890 (2004)
72. Zeng, W., Liu, G.R.: Smoothed finite element methods (S-FEM): An overview and recent developments. Archives of Computational Methods in Engineering pp. to appear, (2016). DOI 10.1007/s11831-016-9202-3
73. Zhang, Z.Q., Liu, G.R., Khoo, B.C.: Immersed smoothed finite element method for two dimensional fluid–structure interaction problems. International Journal for Numerical Methods in Engineering **90**(10), 1292–1320 (2012)
74. Zhang, Z.Q., Liu, G.R., Khoo, B.C.: A three dimensional immersed smoothed finite element method (3D IS-FEM) for fluid–structure interaction problems. Computational Mechanics **51**(2), 129–150 (2013)
75. Zhang, Z.Q., Yao, J., Liu, G.R.: An immersed smoothed finite element method for fluid–structure interaction problems. International Journal of Computational Methods **8**(4), 747–757 (2011)
76. Zhou, C.Y., So, R.M.C., Lam, K.: Vortex-induced vibrations of an elastic circular cylinder. Journal of Fluids and Structures **13**(2), 165–189 (1999)
77. Zienkiewicz, O.C., Nithiarasu, P., Codina, R., Vazquez, M., Ortiz, P.: The characteristic-based-split procedure: An efficient and accurate algorithm for fluid problems. International Journal for Numerical Methods in Fluids **31**(1), 359–392 (1999)
78. Zienkiewicz, O.C., Taylor, R.L., Nithiarasu, P.: The Finite Element Method for Fluid Dynamics, vol. 3, 7th edition edn. Butterworth-Heinemann, Oxford, UK (2014)

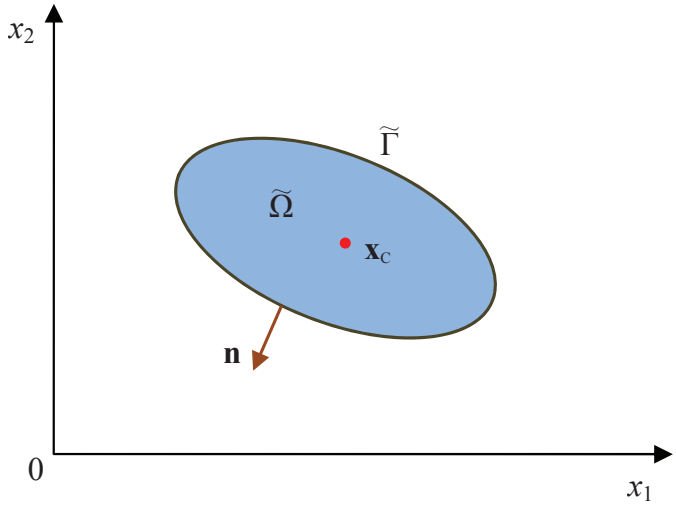

Fig. 1 Illustration of a generic smoothing cell for an arbitrary point.

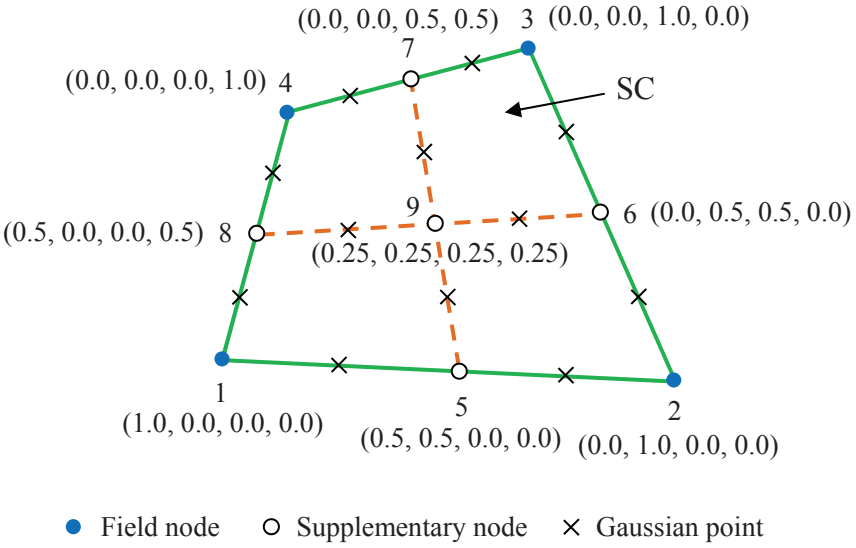

Fig. 2 Construction of SCs and shape functions in a Q4 element.

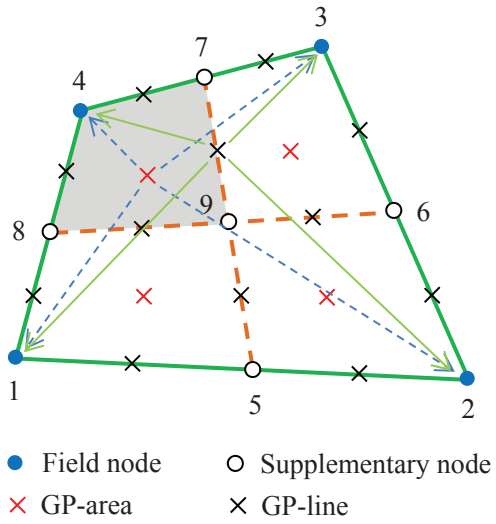

Fig. 3 Contribution of SCs and GPs for Q4 element integral.

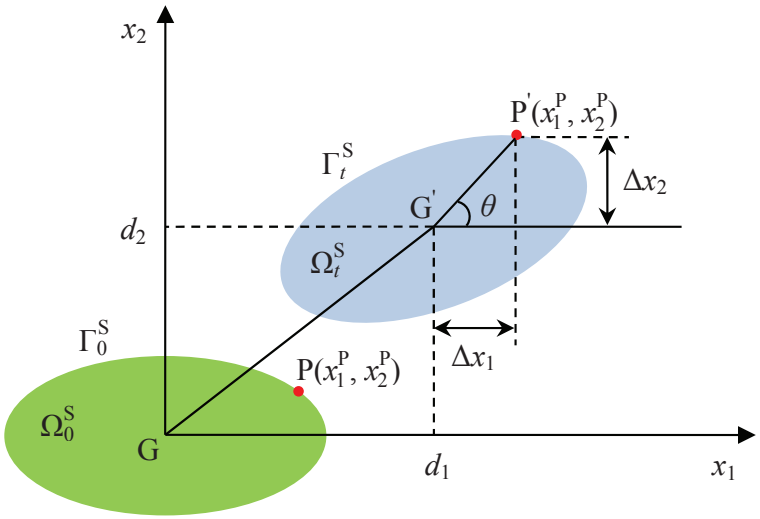

Fig. 4 Schematic view of the generalized planar rigid–body motion.

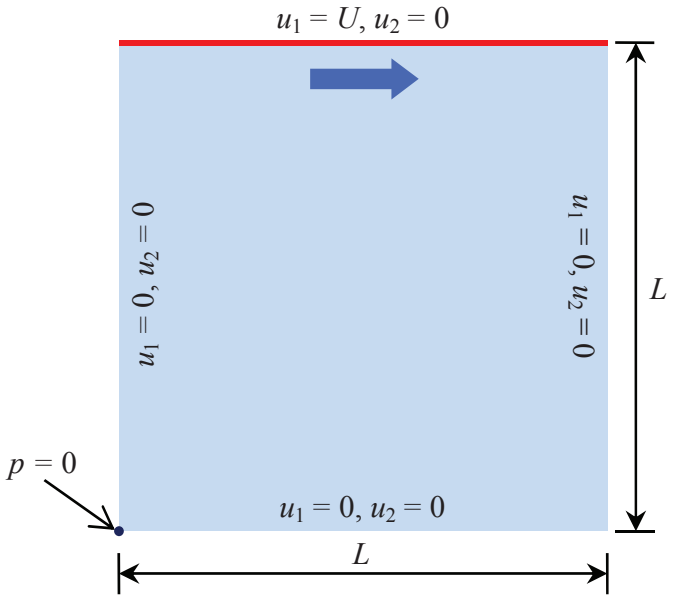

(a) Schematic view

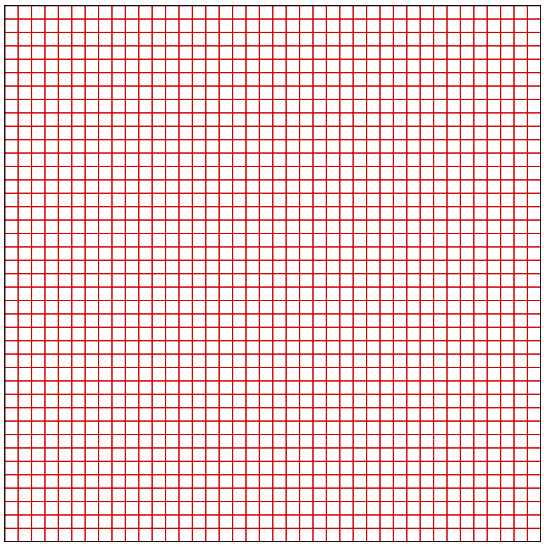

(b) Finite element mesh

Fig. 5 The lid-driven cavity flow.

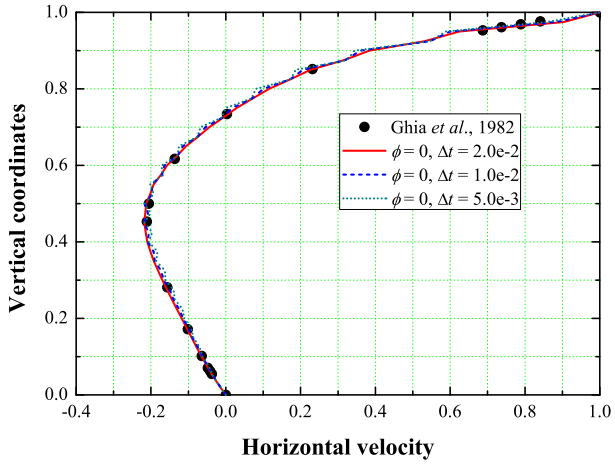

(a) Horizontal velocity along mid-vertical line.

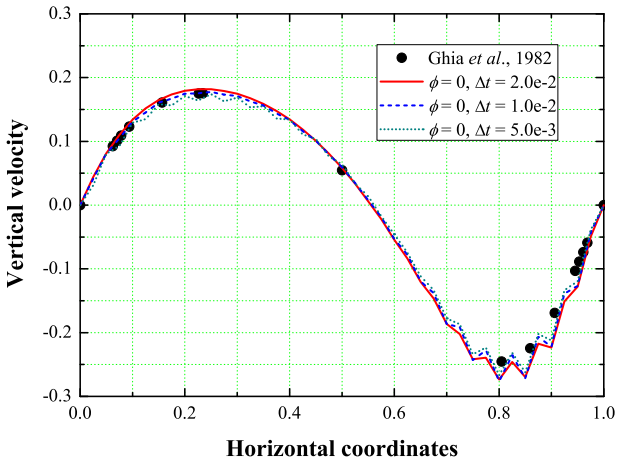

(b) Vertical velocity along mid-horizontal line.

Fig. 6 The $Re = 100$ cavity flow without SPGP stabilization.

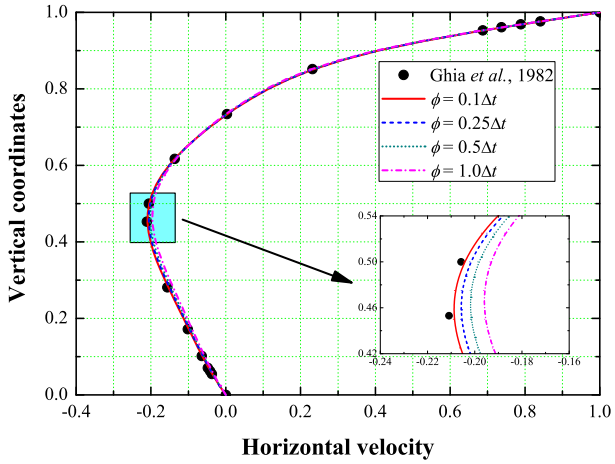

(a) Horizontal velocity along mid-vertical line.

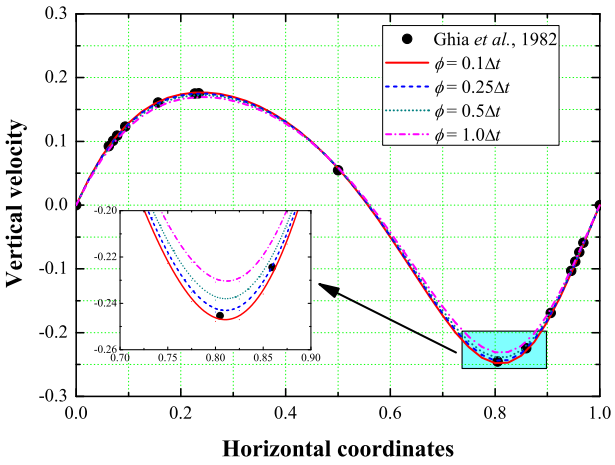

(b) Vertical velocity along mid-horizontal line.

Fig. 7 The $Re = 100$ cavity flow with SPGP stabilization.

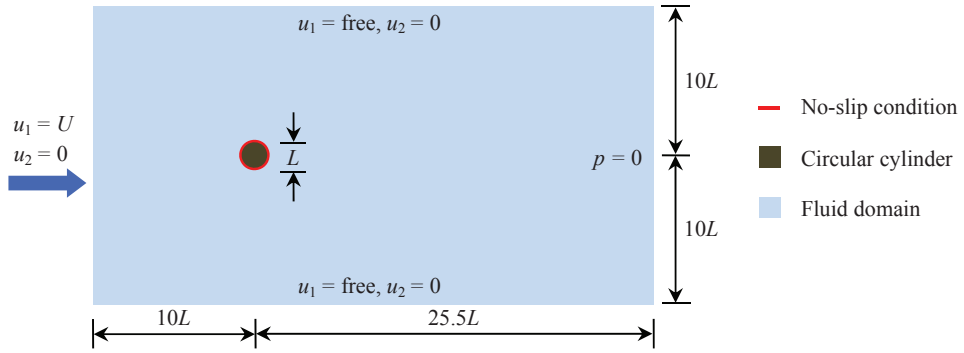

(a) Schematic view.

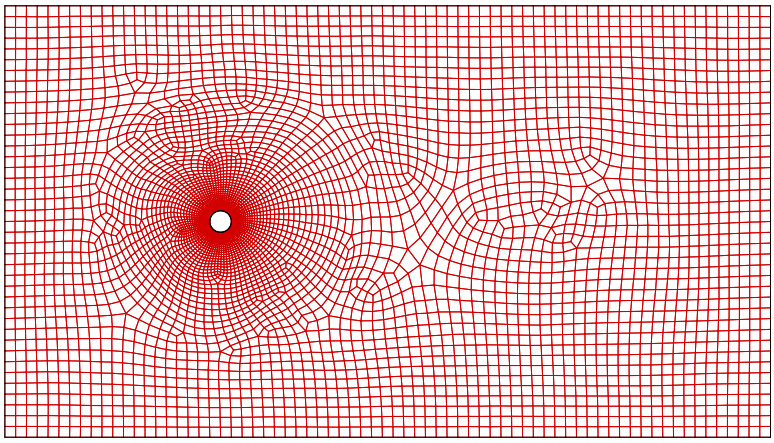

(b) Finite element mesh.

Fig. 8 Flow past a rigid circular cylinder.

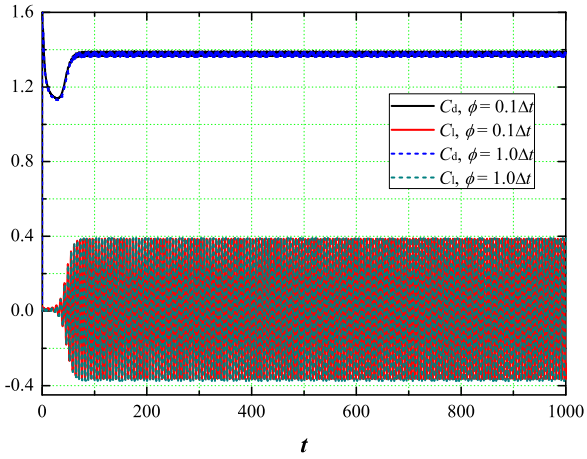

(a) Full-size view.

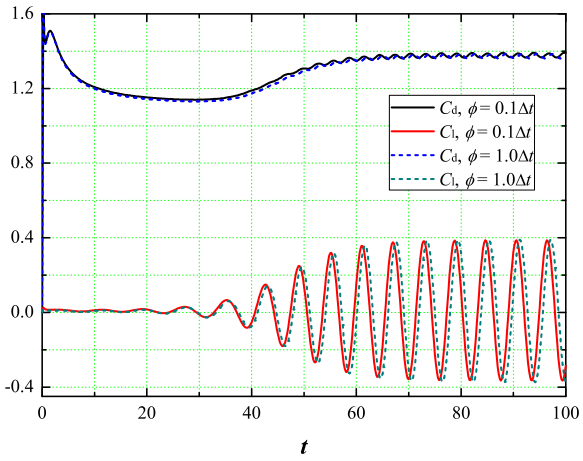

(b) Zoom-in view.

Fig. 9 Time history of drag and lift coefficients.

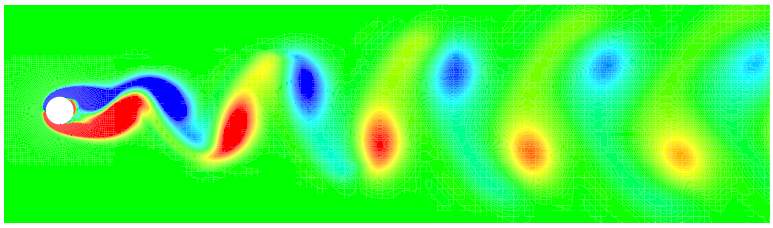

Fig. 10 Vorticity contour of the rigid circular cylinder at $Re = 100$.

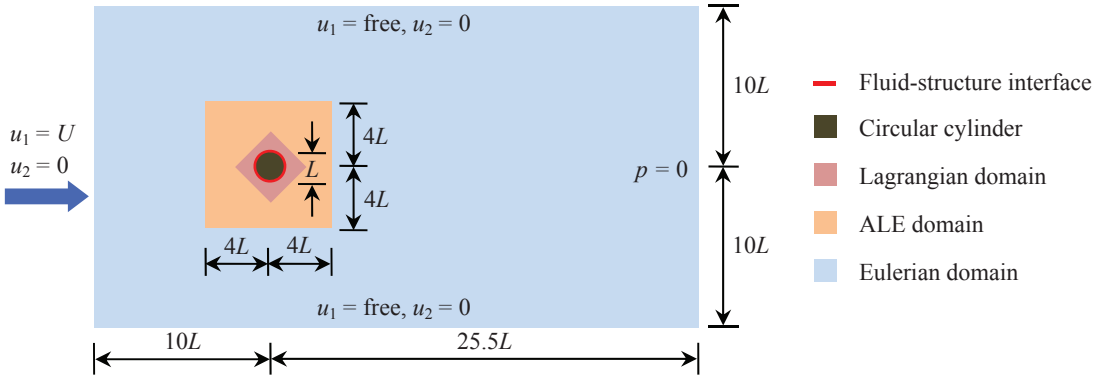

Fig. 11 Sketch of geometry and boundary conditions for the freely oscillating circular cylinder.

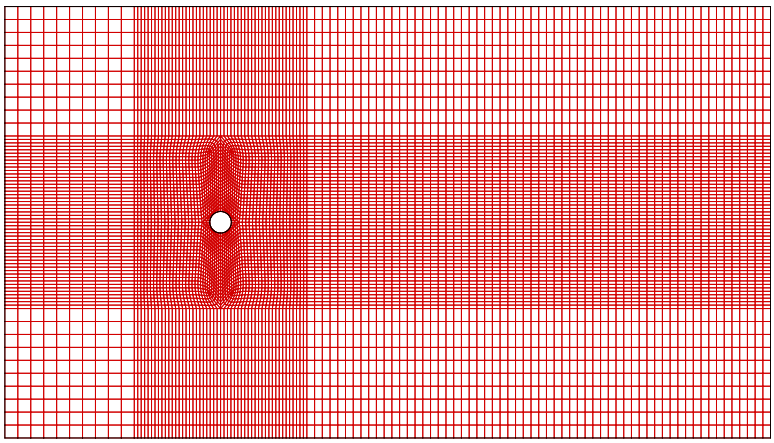

(a) Finite element mesh for the fluid field.

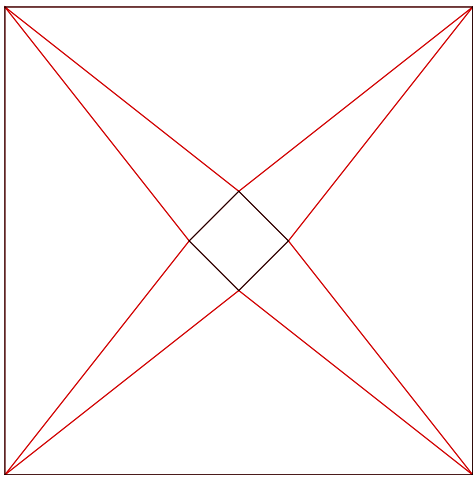

(b) MSA submesh for the ALE domain.

Fig. 12 Snapshots of mesh and submesh of the cylinder problem.

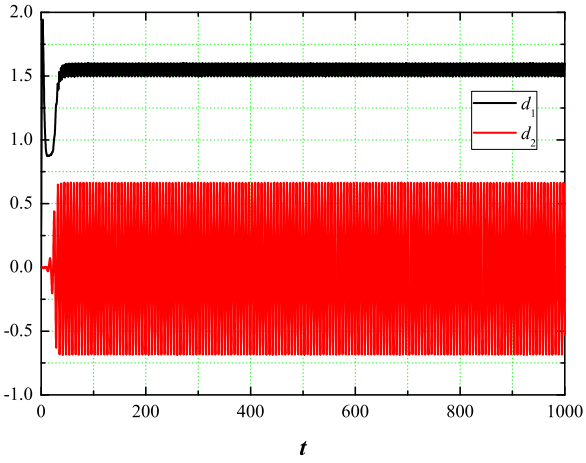

(a) Cylinder displacement.

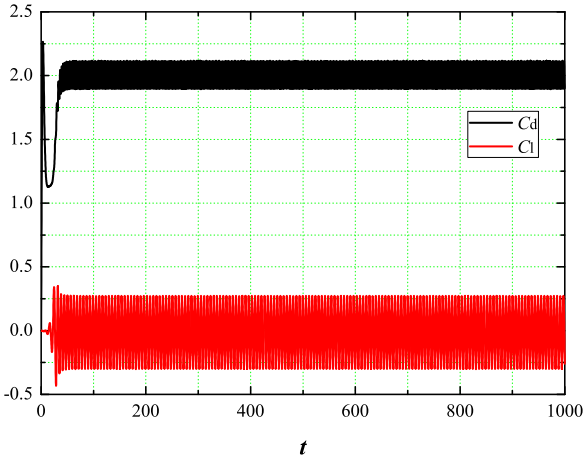

(b) Fluid force coefficients.

Fig. 13 Time history of aerodynamic parameters at $\hat{m} = 0.408$.

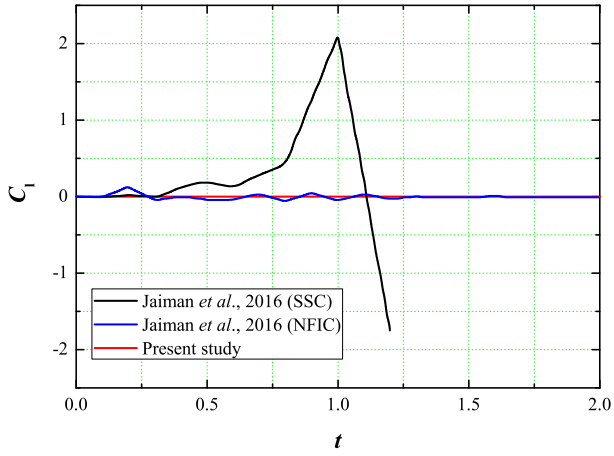

(a) Zoom-in view.

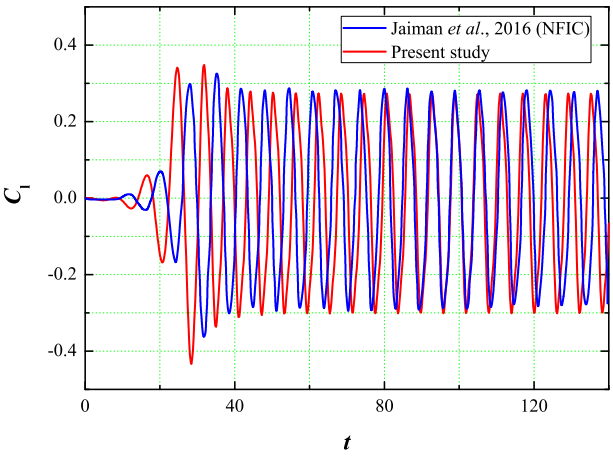

(b) Full-size view.

Fig. 14 Time history of lift coefficient at $\hat{m} = 0.408$.

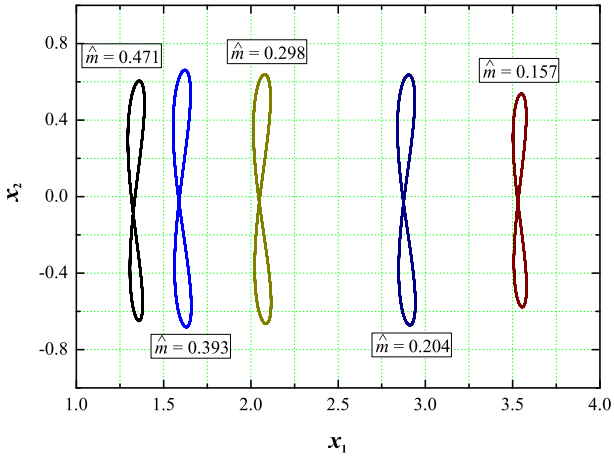

Fig. 15 8-profile trajectory of the oscillating circular cylinder at different $\hat{m}$.

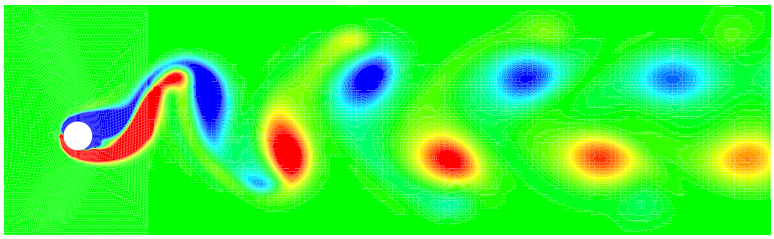

(a) $\hat{m} = 0.393$

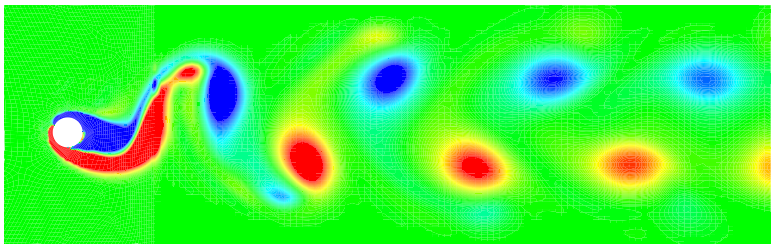

(b) $\hat{m} = 0.298$

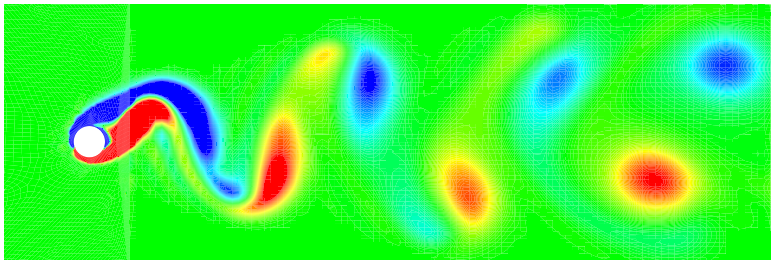

(c) $\hat{m} = 0.157$

Fig. 16 Vorticity contours of the oscillating circular cylinder at various $\hat{m}$.

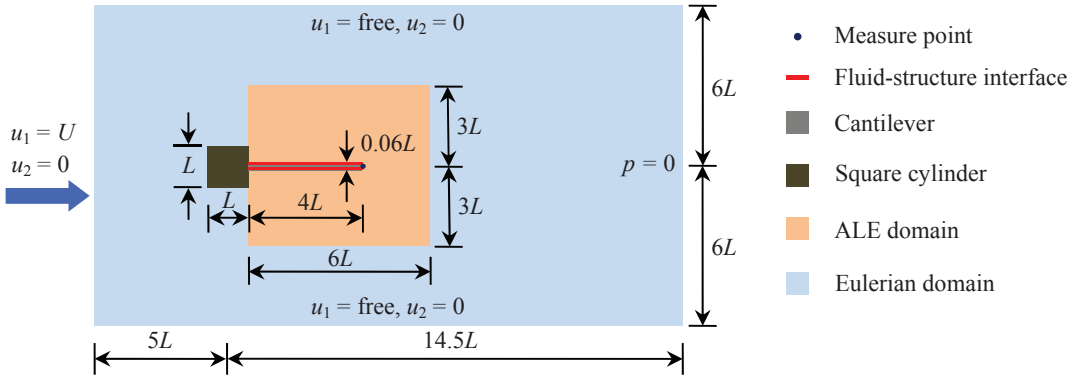

Fig. 17 Sketch of geometry and boundary conditions for a beam attached to a square cylinder.

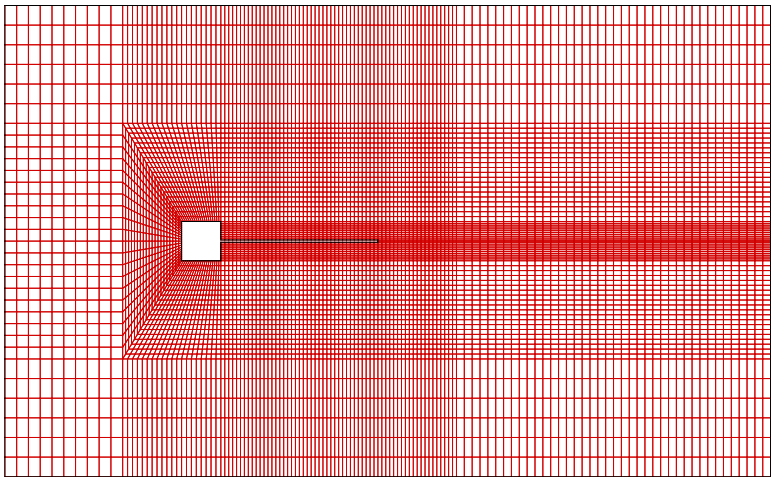

(a) Finite element mesh for the fluid field.

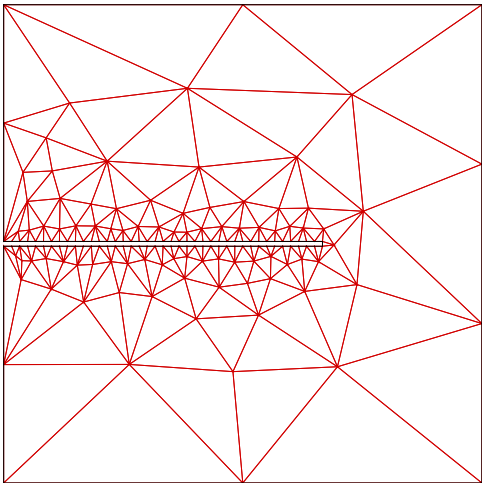

(b) MSA submesh for the ALE domain.

Fig. 18 Snapshots of mesh and submesh of the beam problem.

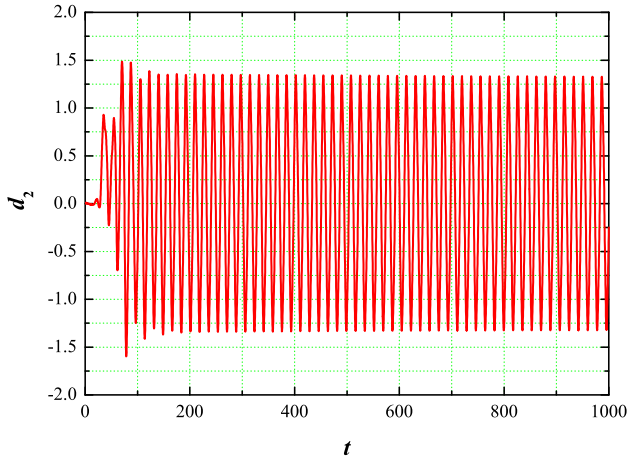

(a) Full-size view.

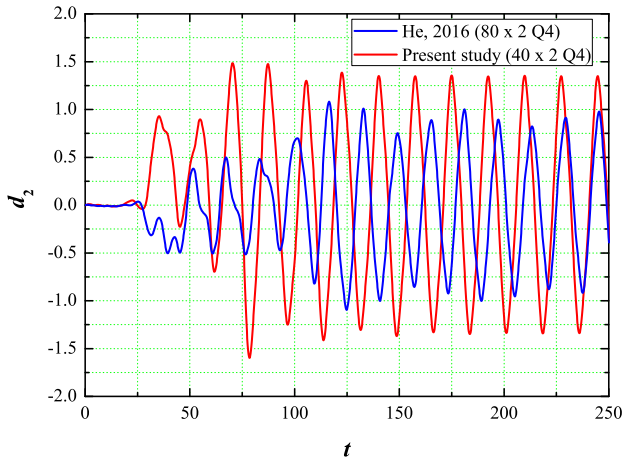

(b) Zoom-in view.

Fig. 19 Time history of vertical displacement at the measuring point.

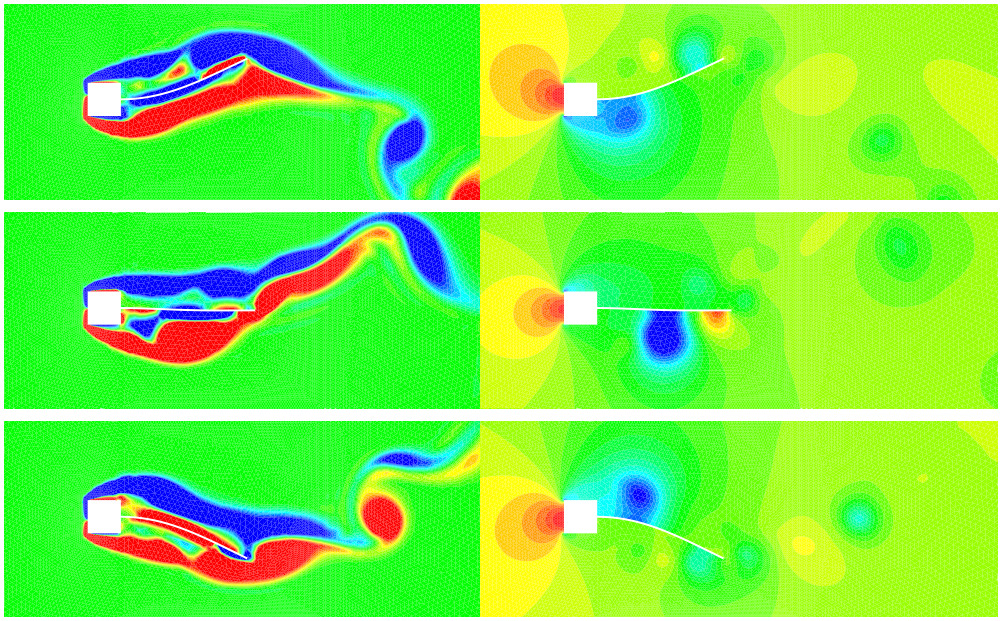

(a) Vorticity. (b) Pressure.

Fig. 20 Instantaneous contours of the beam problem.

Table 1 Collection of run times for the cavity flow.

ϕ	$0.1\Delta t$	$0.25\Delta t$	$0.5\Delta t$	$1.0\Delta t$
run time (s)	1528.3	1509.2	1560.1	1598.5

Table 2 Comparison of the previous and present results for the flow past a circular cylinder.

Reference		$C_{\mathrm{d,mean}}$	$C_{\mathrm{d,rmse}}$	$C_{\mathrm{l,max}}$	$C_{\mathrm{l,rmse}}$	St
Karniadakis [22]		1.42	0.00504	N/A	0.26	0.17
Tezduyar et al. [66]		$1.38 \sim 1.43$	N/A	$0.357 \sim 0.375$	N/A	$0.166 \sim 0.17$
Behr et al. [5]		$1.3698 \sim 1.4552$	N/A	$0.3706 \sim 0.3946$	N/A	$0.1624 \sim 0.1711$
Kjellgren [42]		$1.34 \sim 1.37$	N/A	$0.292 \sim 0.329$	N/A	$0.16 \sim 0.17$
Norberg [56]		N/A	N/A	0.32	N/A	0.164
He et al. [32]		$1.373 \sim 1.421$	$0.00757 \sim 0.01368$	$0.355 \sim 0.489$	$0.251 \sim 0.344$	$0.166 \sim 0.169$
Bevan et al. [6]		N/A	N/A	$0.332 \sim 0.346$	N/A	$0.166 \sim 0.167$
Present study	$\phi = 0$	1.8456	0.01531	0.4190	0.2652	0.1697
	$\phi = 0.1\Delta t$	1.3782	0.00853	0.3880	0.2663	0.1697
	$\phi = 0.25\Delta t$	1.3710	0.00857	0.3869	0.2667	0.1697
	$\phi = 0.5\Delta t$	1.3704	0.00869	0.3880	0.2681	0.1697
	$\phi = 1.0\Delta t$	1.3739	0.00888	0.3912	0.2711	0.1697

Table 3 Collection of run times for the flow past a circular cylinder.

ϕ	$0.1\Delta t$	$0.25\Delta t$	$0.5\Delta t$	$1.0\Delta t$
run time (s)	17923.3	15832.9	18793.9	18868.3

Table 4 Parametric study for the oscillating circular cylinder at $\hat{m} = 0.471$.

ϕ	d_{mean1}	d_{rmse1}	d_{max2}	$C_{\text{d,mean}}$	$C_{\text{d,rmse}}$	$C_{\text{l,max}}$	St	run time (s)
0	N/A	N/A	N/A	N/A	N/A	N/A	N/A	N/A
$0.1\Delta t$	1.2270	0.0203	0.5376	1.8261	0.0495	0.2974	0.1624	33346.4
$0.25\Delta t$	1.2621	0.0240	0.5855	1.8793	0.0611	0.2948	0.1648	29873.3
$0.5\Delta t$	1.2938	0.0269	0.6161	1.9256	0.0711	0.2977	0.1672	30933.8
$1.0\Delta t$	1.3435	0.0306	0.6508	1.9997	0.0834	0.3040	0.1697	30028.4

Table 5 Information on the mesh and submesh generation.

Subsystem	Meshing item	
Fluid	Element type	Q4
	Number of elements	9080
	Number of nodes	9344
Solid	Element type	Q4
	Number of elements	80
	Number of nodes	123
Submesh	Element type	T3
	Number of elements	246
	Number of nodes	170

Table 6 Parametric study for the beam behind an obstacle.

ϕ	$d_{\max 2}$	f_{o}	run time (s)
0	1.31	0.0582	37790.6
$0.1\Delta t$	1.33	0.0582	37932.1
$0.25\Delta t$	1.34	0.0582	38985.7
$0.5\Delta t$	1.35	0.0582	37858.8
$1.0\Delta t$	1.34	0.0582	37566.9

Table 7 Comparison of the present and previous results for the beam behind an obstacle.

Reference	Dimension	Coupling scheme	$d_{\max 2}$	f_{o}
Wall and Ramm [67]	Two	Explicit	1.20	0.0604
Teixeira and Awruch [61]	Three	Explicit	1.35	0.0584
Dettmer and Perić [17]	Two	Implicit	1.25	0.0634
Liew *et al.* [47]	Two	Monolithic	1.34	0.0609
Bazilevs *et al.* [3]	Two	Monolithic	1.21	0.0591
Braun and Awruch [7]	Three	Explicit	$1.181 \sim 1.215$	0.0591
Kassiotis *et al.* [41]	Two	Implicit	1.07	N/A
Habchi *et al.* [23]	Two	Implicit	1.02	0.0634
De Rosis *et al.* [15]	Two	Explicit	1.08	N/A
Froehle and Persson [20]	Two	Implicit	1.12	0.0620
He [25] (20×1 Q9)	Two	Explicit	1.32	0.0586
He [28] (20×1 Q9)	Two	Semi-implicit	1.37	0.0586
He [28] (80×2 Q4)	Two	Semi-implicit	0.92	0.0622
Kaneko *et al.* [40]	Two	Implicit	1.10	0.0624
Present study	Two	Implicit	1.34	0.0582